Analytical Methods

Accepted Manuscript

This article can be cited before page numbers have been issued, to do this please use: F. E. Ogulewe, A. A. Oladipo and M. Gazi, *Anal. Methods*, 2026, DOI: 10.1039/D6AY00358C.

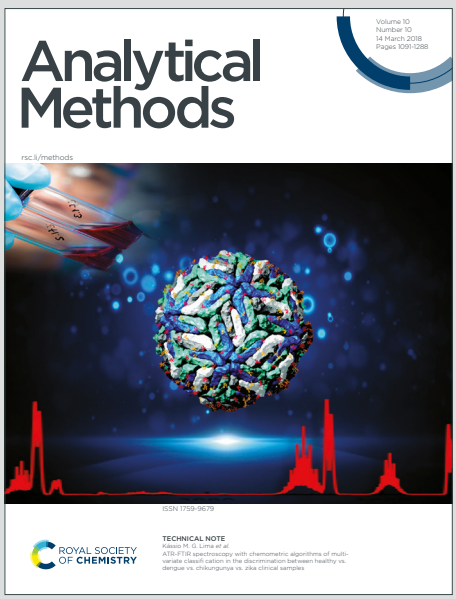

ROYAL SOCIETY OF CHEMISTRY

rsc.li/methods

View Article Online
DOI: 10.1039/D6AY00358C

Nanomaterial-Enhanced Molecular Recognition: A Co_3O_4/TiO_2 Heterojunction Electrochemical Sensor for Vanillin with Experimental and DFT Insights

Favour Ezinne Ogulewe, Akeem Adeyemi Oladipo*, Mustafa Gazi

Polymeric Materials Research Laboratory, Chemistry Department, Faculty of Arts and Science, TR North Cyprus, Eastern Mediterranean University, Famagusta via Mersin 10, Türkiye

*Corresponding authors: akeem.oladipo@emu.edu.tr; akeem.oladipo@gmail.com
F.E.O: https://orcid.org/0009-0006-0100-0696
A.A.O: https://orcid.org/0000-0003-3715-5922
M.G: https://orcid.org/0000-0001-7736-752X

Abstract

An advanced molecularly imprinted electrochemical sensor based on a Co_3O_4/TiO_2 p–n heterojunction nanocomposite was developed for the selective determination of vanillin in complex food matrices. In this novel sensing platform, the heterostructured oxide core provides efficient interfacial charge transfer for enhanced sensitivity, while a surface-confined acrylamide-based molecularly imprinted polymer (MIP) introduces superior molecular recognition and antifouling capabilities. Structural and surface analyses confirmed successful heterojunction formation and polymer integration without electrical insulation of the active sites. Electrochemical characterization revealed a pronounced synergistic effect between the nanocomposite and the MIP, resulting in a substantial reduction in charge-transfer resistance and preservation of the electroactive surface area. Consequently, the sensor exhibited a wide linear range from 2.5 to 250 μM and a low detection limit of 0.06 μM using cyclic voltammetry. Density functional theory (DFT) and Monte Carlo adsorption simulations demonstrated that vanillin forms a highly stable hydrogen-bonding network with acrylamide at an optimal 1:3 ratio. Crucially, the calculated binding energies significantly exceeded those of common interferents such as glucose and ascorbic acid, providing a robust mechanistic basis for the sensor's high selectivity. The sensor was successfully applied to milk, ice cream, biscuits, coffee, and iced tea, delivering recoveries of 96.8–103.2% and excellent agreement with HPLC and UV–Vis methods. The platform retained over 89% of its initial response after 42 days under refrigerated storage. This work establishes a rationally designed, DFT-supported MIP/nanocomposite heterojunction strategy for robust electrochemical sensing in chemically aggressive matrices, highlighting the immense potential of hybrid nanomaterials in analytical applications.

Keywords: Vanillin detection; Molecularly imprinted polymer; p–n heterojunction; Electrochemical sensor; Density functional theory; Structure–property relationship

View Article Online
DOI: 10.1039/D6AY00358C

1. Introduction

Vanillin (4-hydroxy-3-methoxybenzaldehyde) is one of the most extensively used flavoring agents in the global food, beverage, and pharmaceutical industries. Beyond its organoleptic importance, vanillin is widely recognized as a critical quality and authenticity marker, particularly for distinguishing natural vanilla extracts from synthetic vanillin. This distinction is of major regulatory and commercial interest due to the substantial price difference between natural and synthetic products and the widespread occurrence of economic adulteration [1,2]. Although vanillin is generally regarded as safe, excessive consumption of synthetic vanillin has been associated with adverse effects such as headaches, nausea, and hepatic disturbances. Accordingly, the World Health Organization (WHO) and the Joint FAO/WHO Expert Committee on Food Additives (JECFA) have established an acceptable daily intake (ADI) of 0–10 mg kg^{-1} body weight [3]. These regulatory limits necessitate analytical methods capable of accurately determining vanillin concentrations—typically reported to range from approximately 10 to 500 mg kg^{-1} in commercial food products—to ensure compliance, consumer protection, and food safety.

Despite the availability of established analytical techniques, the accurate quantification of vanillin in real food samples remains challenging, primarily due to the chemically aggressive and heterogeneous nature of food matrices. Conventional chromatographic methods such as high-performance liquid chromatography (HPLC) and gas chromatography–mass spectrometry (GC–MS) offer excellent sensitivity and selectivity; however, they are often labor-intensive, costly, and unsuitable for rapid or on-site screening. Electrochemical sensors represent an attractive alternative owing to their simplicity, portability, and rapid response. Nevertheless, their application to complex food matrices—including coffee, high-fat dairy products, and protein-rich formulations—remains severely limited. In such systems, electrode surfaces are prone to fouling

View Article Online
DOI: 10.1039/D6AY00358C

by macromolecules such as proteins and lipids, while structurally related electroactive compounds (e.g., phenolic acids and catechol derivatives) generate non-specific oxidation signals that overlap with the electrochemical response of vanillin [4]. Consequently, the development of sensing platforms that integrate high electrocatalytic efficiency with robust molecular selectivity is not merely advantageous but analytically essential.

In recent years, the integration of functional polymers and nanostructured metal oxides has driven significant advancements across diverse analytical platforms. Recent literature prominently highlights the exceptional utility of specifically engineered nanocomposites—such as polymer-functionalized TiO_2 matrices, bimetallic MOFs, shape-controlled Co_3O_4 architectures, and multi-component nanomaterial assemblies—in achieving breakthrough sensitivities for food safety monitoring, clinical biomarker detection, and environmental analysis [5–13]. Building upon these advanced nanomaterial paradigms, we targeted the synergistic integration of specific transition metal oxides for our sensor design.

To overcome the intrinsic sensitivity limitations of bare electrodes, transition metal oxides have been extensively explored as electrocatalytic modifiers. Tricobalt tetraoxide (Co_3O_4), a p-type semiconductor, exhibits remarkable redox activity arising from the coexistence of Co^{2+} and Co^{3+} species, which significantly enhances electron transfer kinetics for the oxidation of organic analytes [14–17]. However, pristine Co_3O_4 suffers from aggregation tendencies and limited electrochemical conductivity during prolonged operation. Titanium dioxide (TiO_2), an n-type semiconductor, is widely valued for its chemical inertness, structural stability, and surface hydroxyl groups, making it an ideal stabilizing support material. The integration of p-type Co_3O_4 with n-type TiO_2 leads to the formation of a p–n heterojunction. Upon contact, the disparate work functions of the two materials drive the equilibration of their Fermi levels, establishing a built-in

View Article Online
DOI: 10.1039/D6AY00358C

internal electric field at the interface. This internal field effectively accelerates interfacial charge separation, dramatically lowers charge-transfer resistance, and suppresses electron–hole recombination. Consequently, this synergistic interaction results in an amplified electrochemical response and improved signal stability that far exceeds the individual sensing capabilities of the single metal oxides [18].

While nanostructured materials significantly enhance sensitivity [15,19,20], selectivity in complex matrices cannot be guaranteed by electrocatalysis alone. Molecular Imprinting Technology (MIT) provides a powerful strategy to introduce molecular recognition into electrochemical sensors. Molecularly imprinted polymers (MIPs) are synthesized in the presence of a template molecule, generating recognition cavities with complementary shape, size, and functional group orientation to the target analyte [21,22]. Despite the growing number of vanillin sensors reported in the literature, a critical limitation persists: the interaction between the metal oxide support and the MIP recognition layer is frequently optimized empirically, with little mechanistic understanding. In particular, atomic-level insights into vanillin adsorption at heterojunction–MIP interfaces are rarely reported, resulting in a largely "black-box" design approach that hampers rational sensor development.

In this work, we report the fabrication of a highly selective electrochemical sensor based on a Co_3O_4/TiO_2 nanocomposite functionalized with a molecularly imprinted polymer for the determination of vanillin in complex food matrices. The novelty of this study lies in the **synergistic integration of heterojunction-driven electrocatalysis and molecular imprinting–based selectivity**, supported by both comprehensive experimental validation and density functional theory (DFT) calculations. Unlike conventional sensor studies that rely primarily on standard solution testing, the present work adheres to stringent analytical validation criteria: endogenous

View Article Online
DOI: 10.1039/D6AY00358C

vanillin is detected in unspiked food samples, interference studies are conducted using concentration ratios representative of real matrices, and long-term stability is evaluated over 42 days under different storage conditions. Furthermore, DFT modeling is employed to calculate adsorption energies (E_{ads}) and elucidate the preferred binding geometry of vanillin at the MIP interface, providing a theoretical basis for the observed analytical performance. This integrated experimental–theoretical approach enables reliable vanillin determination across diverse food matrices, ranging from brewed coffee to high-fat ice cream, demonstrating the practical applicability of the proposed sensor for modern food quality control and safety monitoring.

2. Experimental Section

2.1. Materials and Reagents

All reagents were of analytical grade and used without further purification. Cobalt(II) nitrate hexahydrate ($Co(NO_3)_2 \cdot 6H_2O$), titanium(IV) oxide (TiO_2, anatase), acrylamide, 2,2′-azobisisobutyronitrile (AIBN), potassium ferricyanide ($K_3[Fe(CN)_6]$), potassium ferrocyanide ($K_4[Fe(CN)_6]$), monopotassium phosphate (KH_2PO_4), disodium phosphate ($Na_2HPO_4 \cdot 7H_2O$), citric acid, calcium chloride ($CaCl_2$), sodium chloride (NaCl), potassium chloride (KCl), sodium hydroxide (NaOH), benzaldehyde, 2,4,5-trichlorophenol, sodium sulfate (Na_2SO_4), acetic acid, methanol, and acetonitrile were purchased from Merck KGaA (Darmstadt, Germany). D-glucose, fructose, sucrose, and magnesium chloride hexahydrate ($MgCl_2 \cdot 6H_2O$) were obtained from Philip Harris. Vanillin (≥99%), ethylene glycol dimethacrylate (EGDMA), and Nafion perfluorinated resin solution (5 wt%) were procured from Sigma-Aldrich (Steinheim, Germany). Phosphate-buffered saline (PBS, 0.1 M) was prepared from KH_2PO_4, Na_2HPO_4, NaCl, and KCl, with pH adjusted using 0.1 M NaOH or HCl. All aqueous solutions were prepared using ultrapure water (18.2 MΩ·cm). Commercial food samples (vanilla-flavored iced tea, milk, ice cream, protein

View Article Online
DOI: 10.1039/D6AY00358C

powder, and biscuits) were obtained from local retail markets and analyzed before their expiration dates.

2.2.Synthesis of Co_3O_4/TiO_2 Nanocomposite

The Co_3O_4/TiO_2 heterojunction nanocomposite was synthesized via a controlled hydrothermal deposition followed by thermal oxidation. Initially, 1.0 g of commercial TiO_2 powder was dispersed in 30 mL of deionized water and ultrasonicated for 30 min to ensure complete de-agglomeration. Separately, a cobalt precursor solution was prepared by dissolving 2.0 g of $Co(NO_3)_2 \cdot 6H_2O$ and 0.6 g of NaOH in 30 mL of deionized water. The cobalt solution was added dropwise to the TiO_2 suspension under vigorous stirring (500 rpm), followed by continuous stirring for 1 h to promote homogeneous nucleation of cobalt hydroxide on the TiO_2 surface. The resulting mixture was transferred to a 100 mL Teflon-lined stainless-steel autoclave and hydrothermally treated at 150 °C for 12 h. After cooling, the precipitate was collected by centrifugation (3500 rpm, 5 min), washed sequentially with deionized water and ethanol (three cycles each), and dried at 80 °C for 17 h. The dried powder was finely ground and calcined at 400 °C for 2 h in air, yielding a crystalline black Co_3O_4/TiO_2 nanocomposite with a stabilized p–n heterojunction architecture.

2.3.Fabrication of the Molecularly Imprinted Composite

The molecularly imprinted polymer (MIP) was synthesized via bulk thermal polymerization directly incorporating the Co_3O_4/TiO_2 nanocomposite. This chemical polymerization route was specifically selected over electropolymerization to generate a highly cross-linked, rigid 3D framework capable of uniformly encapsulating the metal oxides, maximizing the volumetric density of recognition cavities, and providing the necessary mechanical robustness to withstand severe fouling in complex food matrices. Vanillin (0.3 mM, template) and acrylamide (1.2 mM, functional monomer) were dissolved in 10 mL acetonitrile to allow noncovalent pre-complex

View Article Online
DOI: 10.1039/D6AY00358C

formation via hydrogen bonding. The solution was sonicated at 5 °C for 30 min to stabilize the template–monomer interactions. Subsequently, 0.25 g of the Co_3O_4/TiO_2 nanocomposite was dispersed into the pre-polymerization mixture, followed by the addition of EGDMA (4.5 mM, cross-linker) and AIBN (0.37 mM, initiator). The suspension was purged with nitrogen for 10 min to remove dissolved oxygen, sealed, and polymerized at 70 °C under continuous stirring.

To empirically optimize the polymer shell thickness and prevent mass-transport limitations, a kinetic study was conducted evaluating polymerization times from 12 to 36 h, with 24 h ultimately selected as the optimum duration. The resulting polymer composite was dried at 60 °C, ground, and sieved to obtain a uniform powder. Template removal was performed using Soxhlet extraction with methanol/acetic acid (8:2, v/v) at 80 °C for 8 h until vanillin was no longer detectable in the extract. The final $MIP/Co_3O_4/TiO_2$ material was washed with methanol and dried under vacuum. A non-imprinted polymer (NIP) was prepared following the same procedure in the absence of vanillin.

2.4.Electrode Modification

A glassy carbon electrode (GCE, 3 mm diameter) was sequentially polished with 0.3 μm and 0.05 μm alumina slurries, rinsed thoroughly with deionized water, and dried under nitrogen. A modification ink was prepared by dispersing 2.0 mg of $MIP/Co_3O_4/TiO_2$ powder in a mixture of 0.8 mL deionized water, 0.2 mL ethanol, and 10 μL Nafion (5 wt%). The suspension was sonicated for 20 min at 10 °C. A 5 μL aliquot was drop-cast onto the cleaned GCE surface and dried under an infrared lamp for 20 min; this process was repeated twice to ensure uniform film formation. The resulting electrode is denoted as $MIP/Co_3O_4/TiO_2/GCE$.

View Article Online
DOI: 10.1039/D6AY00358C

2.5.Real Sample Pretreatment

To assess analytical performance under realistic conditions, five food matrices of increasing complexity were analyzed. To rigorously evaluate matrix effects, vanillin spiking was performed prior to any extraction or pretreatment steps.

- **Complex liquid matrices** (milk, ice cream, coffee, protein shake): Protein and lipid precipitation was achieved using cold acetonitrile. ACN-to-sample ratios of 2:1 (v/v) were applied for milk, coffee, and ice cream, while a 4:1 ratio was used for the protein shake. Samples were vortexed for 1 min and centrifuged at 5000 rpm for 15 min.
- **Solid matrices** (biscuits): Samples were finely ground; 1.0 g was extracted with 10 mL methanol/water (70:30, v/v), ultrasonicated for 30 min, and centrifuged.
- **Simple liquid matrices** (iced tea): Samples were directly filtered without precipitation.

All supernatants were filtered through 0.45 μm syringe filters and diluted with 0.1 M PBS (pH 7.0) to reduce organic solvent content below 15% prior to electrochemical analysis.

2.6. Electrochemical Measurements

Electrochemical experiments were performed using a CS350M workstation (Corrtest Instruments) in a conventional three-electrode configuration comprising the modified GCE (working electrode), platinum wire (counter electrode), and Ag/AgCl (reference electrode). Electrode characterization was conducted by cyclic voltammetry (CV) and electrochemical impedance spectroscopy (EIS) in 0.1 M KCl containing 2.0 mM $[Fe(CN)_6]^{3-/4-}$. EIS spectra were collected over a frequency range of 100 kHz to 1 Hz. Quantitative determination of vanillin was performed in 0.1 M PBS using the standard addition method to compensate for residual matrix effects. Based on systematic optimization studies, all final quantitative detection of vanillin was performed using cyclic

View Article Online
DOI: 10.1039/D6AY00358C

voltammetry at a scan rate of 50 mV s^{-1} within a potential window of −0.4 V to +0.8 V (vs. Ag/AgCl) in 0.1 M PBS, pH 7.0, following an accumulation time of 6 minutes prior to scanning.

2.7. Reference Analytical Methods

Electrochemical results were validated against UV–Vis spectrophotometry (Hitachi U-3010) and high-performance liquid chromatography (Agilent 1260 Infinity II). UV–Vis measurements were conducted at λ_{max} =280 nm. HPLC analysis employed a C18 column (250 × 4.6 mm, 5 μm) with an isocratic mobile phase of acetonitrile/water (1% acetic acid, 50:50 v/v) at 1.0 mL·min^{-1} and UV detection at 280 nm. Statistical agreement was evaluated using paired *t*-tests and *F*-tests at the 95% confidence level. Detailed metrics are provided in the Supporting Information (S1-S2).

2.8. Computational Details

Density functional theory (DFT) calculations and Monte Carlo (MC) simulations were conducted using BIOVIA Materials Studio (v24.1). Geometry optimizations were performed with the DMol³ code using the generalized gradient approximation (GGA) with the Perdew-Burke-Ernzerhof (PBE) exchange-correlation functional. A double numerical plus polarization (DNP) basis set was employed, which minimizes basis set superposition error (BSSE) compared to standard Gaussian basis sets. To accurately and efficiently describe the localized d-electrons of the transition metals, DFT Semi-core Pseudopotentials (DSPP) were applied. Due to the presence of paramagnetic Co species in the heterojunction, all calculations were spin-polarized (spin-unrestricted). Furthermore, to accurately capture the non-covalent van der Waals interactions critical to molecular imprinting and adsorption, Grimme's empirical dispersion correction (DFT-D) was incorporated.

Convergence criteria were set to 1.0×10^{-5} Ha for energy, 0.002 Ha·$Å^{-1}$ for force, and 0.005 Å for displacement [23]. A global orbital cutoff of 5.0 Å and a self-consistent field (SCF) tolerance

View Article Online
DOI: 10.1039/D6AY00358C

of 1.0×10^{-6} Ha were utilized to ensure high electronic convergence. Binding energies were calculated as:

$$\Delta E_{bind} = E_{complex} - \left(E_{template} + n \times E_{monomer}\right)$$

Adsorption behavior on the Co_3O_4/TiO_2 surface was modeled using the Adsorption Locator module. Simulations were performed under the NVT thermodynamic ensemble at 298 K, employing the COMPASS III force field, which is highly parameterized for complex organic-inorganic interfaces. Adsorption energy was determined as:

$$E_{ads} = E_{total} - \left(E_{surface} + E_{vanillin}\right)$$

where E_{total} represents the total energy of the surface-adsorbate system, while $E_{surface}$ and $E_{vanillin}$ are the energies of the bare surface and the isolated vanillin molecule, respectively.

2.9. Material Characterization

Structural, morphological, and surface analyses were performed using XRD (Rigaku Ultima IV), SEM/EDS (QUANTA 400F), TEM (FEI Tecnai G2), FTIR (PerkinElmer), XPS (PHI 5000), and BET surface area analysis (Quantachrome Autosorb 1C). Detailed instrumental parameters are provided in the Supporting Information.

3. Results and Discussion

The analytical performance of the MIP/Co_3O_4/TiO_2 sensor is dictated by the cooperative interplay between the p–n heterojunction nanocomposite and the surface-confined molecularly imprinted polymer. As illustrated in **Scheme 1**, vanillin forms a pre-polymerization complex with acrylamide through directional hydrogen bonding, which is subsequently immobilized on the Co_3O_4/TiO_2 surface during cross-linked polymer growth and template removal, generating selective recognition cavities. Accordingly, this section progresses from validation of heterojunction formation and interfacial charge-transfer properties to confirmation of imprinting efficiency and

View Article Online
DOI: 10.1039/D6AY00358C

molecular selectivity. Density functional theory (DFT) calculations are integrated throughout as a mechanistic tool to rationalize experimentally observed selectivity, sensitivity, and interference tolerance, directly linking adsorption energetics and binding configurations to electrochemical parameters such as charge-transfer resistance and detection limit.

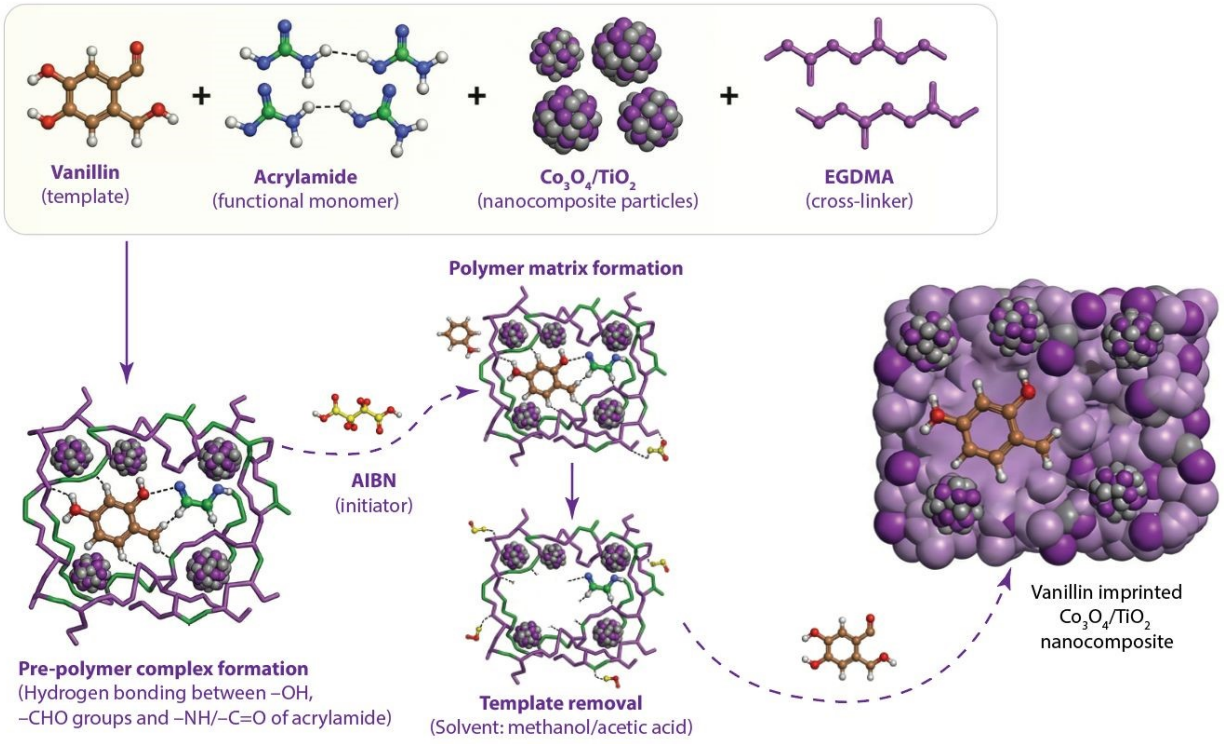

Scheme 1. Schematic illustration of vanillin-imprinted polymer formation on Co_3O_4/TiO_2 nanocomposite via hydrogen-bond-driven pre-polymerization, cross-linking, and template removal.

3.1. Material Architecture and Heterojunction Confirmation

3.1.1. Structural and Morphological Characterization

The crystalline phase composition of the synthesized nanocomposites was first examined by X-ray diffraction (XRD). The diffraction pattern of the non-imprinted Co_3O_4/TiO_2 nanocomposite (Fig.1a) displays well-defined reflections at 2θ = 25.34°, 37.84°, 48.12°, 55.12°, 62.72°, and 75.06°, corresponding to the (101), (004), (200), (211), (204), and (215) planes of anatase TiO_2

View Article Online
DOI: 10.1039/D6AY00358C

(JCPDS No. 21-1272) [24]. Additional characteristic peaks at ~32.09° (220), 36.94° (311), 59.26° (511), and 65.56° (440) are indexed to the cubic spinel Co_3O_4 phase (JCPDS No. 42-1467)[25], confirming the successful integration of both metal oxides without detectable impurity phases.

Quantitative analysis indicates that anatase TiO_2 constitutes the dominant crystalline phase, with an average crystallite size of 57 nm, a dislocation density of 3.08×10^{14} lines m^{-2}, and a microstrain of 0.0029. In contrast, Co_3O_4 is present as a dispersed phase with a smaller crystallite size of 23.1 nm, higher defect density (1.87×10^{15} lines m^{-2}), and increased microstrain (0.0049), reflecting its role as the catalytically active component. The overall crystallinity of the composite reaches 89.9%, consistent with its sharp diffraction features.

Following molecular imprinting, the XRD pattern of the MIP/Co_3O_4/TiO_2 composite retains the characteristic reflections of both oxides, indicating preservation of the inorganic framework. However, a noticeable reduction in peak intensity and broadening is observed, corresponding to a decrease in crystallinity to 72.2%. The average crystallite size of TiO_2 decreases to 39.2 nm, accompanied by increased lattice strain (0.0042) and dislocation density (6.51×10^{14} lines m^{-2}). Similarly, the Co_3O_4 phase exhibits a reduced crystallite size of 14.8 nm and higher defect density (4.56×10^{15} lines m^{-2}). These changes are attributed to confinement effects imposed by the polymer matrix and confirm that the imprinting process effectively modulates the microstructure without disrupting phase integrity.

3.1.2. Transmission Electron Microscopy and SAED Analysis

The microstructural architecture of the nanocomposites was further elucidated using conventional transmission electron microscopy (CTEM) and selected area electron diffraction (SAED). For the non-imprinted Co_3O_4/TiO_2 (Fig.1b and Fig.S1a), bright-field images reveal a heterogeneous morphology consisting of smaller, dark-contrast nanoparticles anchored onto larger, lighter-

View Article Online
DOI: 10.1039/D6AY00358C

contrast grains. Based on Z-contrast considerations (Z_{Co} = 27 vs. Z_{Ti} = 22) and particle size analysis, the darker domains (20–30 nm) are assigned to Co_3O_4, while the larger support grains (~57 nm) correspond to anatase TiO_2.

High-magnification images (Fig.S1a) confirm the formation of a direct, intimate heterojunction interface, with Co_3O_4 domains embedded into or strongly coupled with the TiO_2 lattice rather than simply physically mixed. This structural integration is critical for efficient interfacial charge transfer. The corresponding SAED pattern (Fig.1c) exhibits sharp, concentric diffraction rings with discrete bright spots indexed to anatase TiO_2 planes [26], consistent with the high crystallinity and polycrystalline nature of the composite. In contrast, the MIP/Co_3O_4/TiO_2 nanocomposite (Fig.1d and Fig.S1b) displays a distinct morphological transformation. The inorganic nanoparticles are encapsulated within a continuous, semi-transparent amorphous layer attributed to the acrylamide-based polymer network. This coating restricts crystal growth and promotes moderate agglomeration through polymer cross-linking. The corresponding SAED pattern (Fig.S1c) is dominated by a diffuse central halo characteristic of amorphous materials, while faint diffraction rings from the metal oxide cores remain discernible. This observation corroborates the reduced crystallinity observed by XRD and confirms that the inorganic cores remain structurally intact but are embedded within an amorphous imprinted matrix.

3.1.3. Scanning Electron Microscopy and Surface Morphology

Scanning electron microscopy (SEM) provides complementary insight into surface morphology at the microscale. The pristine Co_3O_4/TiO_2 nanocomposite (Fig.1e) exhibits a rough, highly granular topography composed of loosely aggregated nanoparticles with sharp edges. The resulting disordered stacking generates significant interparticle voids, consistent with its high crystallinity and favorable geometric surface area for electrochemical applications. After molecular imprinting,

View Article Online
DOI: 10.1039/D6AY00358C

the MIP/Co_3O_4/TiO_2 composite (Fig.1f) shows a pronounced change in surface texture. The sharp granular features are softened and appear more cohesive, reflecting encapsulation by the polymer network. Importantly, the material retains a three-dimensional, coral-like porous architecture with interconnected macroporous channels. This confirms that polymerization yields a permeable recognition scaffold rather than a dense insulating film, ensuring continued accessibility of electroactive sites and imprinted cavities. For direct structural comparison, the morphology of the non-imprinted polymer (NIP) was also evaluated (Fig.S2). In contrast to the highly porous, roughened architecture of the MIP layer, the NIP exhibited a noticeably denser and smoother surface. This clear morphological difference provides direct visual confirmation of the successful formation of molecular recognition cavities within the MIP matrix following the extraction of the vanillin template.

Energy-dispersive X-ray (EDX) spectroscopy was employed to confirm the elemental composition and to provide chemical evidence for polymer encapsulation of the Co_3O_4/TiO_2 heterojunction. As shown in Fig. S1d, the non-imprinted Co_3O_4/TiO_2 nanocomposite exhibits clear signals corresponding to C, O, Ti, and Co, with carbon accounting for 16.85 wt%, oxygen 31.84 wt%, titanium 28.06 wt%, and cobalt 18.06 wt%. The presence of Ti and Co at comparable weight fractions confirms the successful integration of both metal oxides within the nanocomposite framework.

Following molecular imprinting, the EDX spectrum of MIP/Co_3O_4/TiO_2 (Fig. S1e) is dominated by a pronounced increase in carbon content to 71.90 wt%, accompanied by a relative decrease in oxygen (21.13 wt%) and substantial attenuation of the Ti (4.13 wt%) and Co (2.84 wt%) signals. This dramatic shift in elemental composition provides direct chemical evidence that the inorganic Co_3O_4/TiO_2 heterojunction is effectively encapsulated within the organic polymer

View Article Online
DOI: 10.1039/D6AY00358C

matrix. The suppressed metal signals indicate shielding by the imprinted polymer layer rather than loss of the inorganic phase, in excellent agreement with SEM and TEM observations showing conformal polymer coverage.

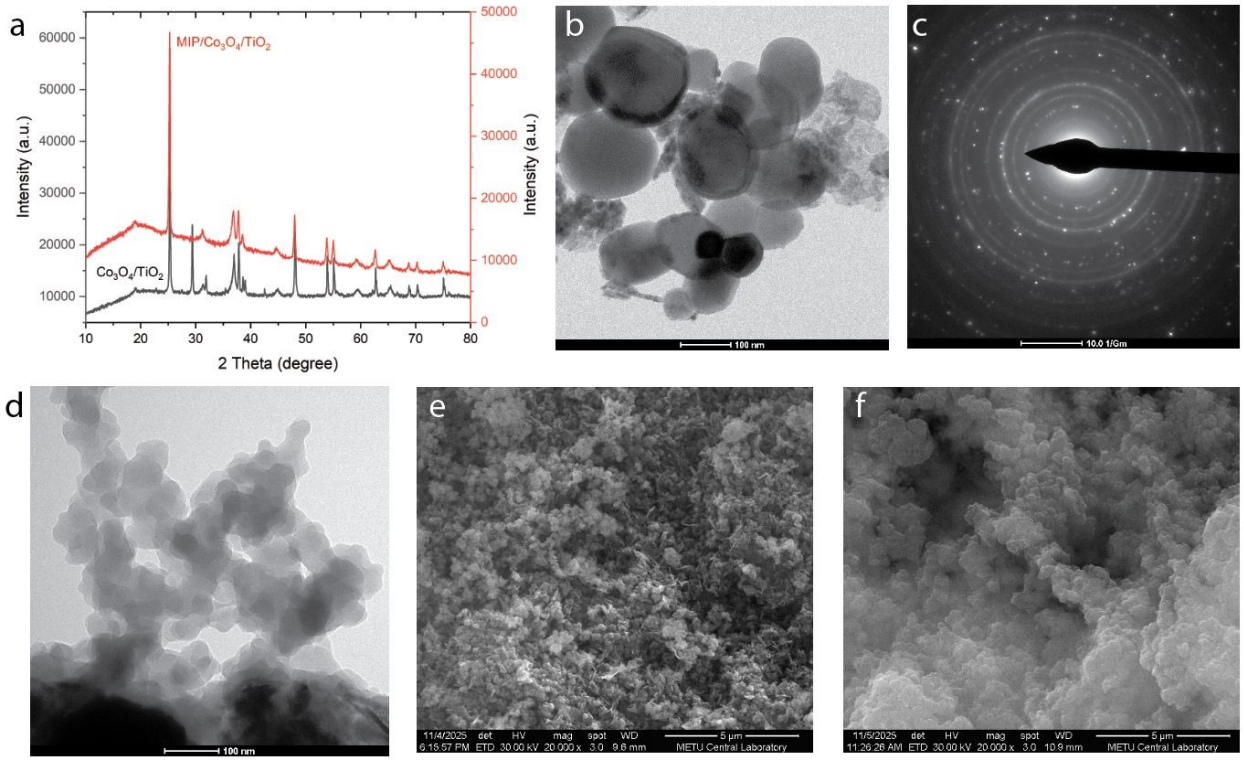

Fig. 1 a XRD patterns **b** TEM image of Co_3O_4/TiO_2 **c** SAED pattern indicating a polycrystalline heterojunction structure **d** TEM image of MIP/Co_3O_4/TiO_2 **e** SEM image of Co_3O_4/TiO_2 **f** SEM image of MIP/Co_3O_4/TiO_2.

3.1.4. FTIR Analysis and Molecular Imprinting Validation

Fourier-transform infrared (FTIR) spectroscopy was employed to monitor surface functionalization and confirm successful molecular imprinting (Fig.2a). The spectrum of pristine Co_3O_4/TiO_2 is dominated by strong absorption bands in the 500–800 cm^{-1} region, corresponding to Co–O and Ti–O–Ti stretching vibrations, confirming the inorganic nature of the core material

View Article Online
DOI: 10.1039/D6AY00358C

[25,27]. A broad band centered at ~3400 cm^{-1} is attributed to surface hydroxyl groups, which serve as anchoring sites for subsequent polymerization.

Upon formation of the molecularly imprinted polymer, the MIP/Co_3O_4/TiO_2 spectrum exhibits pronounced spectral changes indicative of organic encapsulation. A sharp band at 1730 cm^{-1} corresponds to C=O stretching of ester groups from the EGDMA cross-linker, while distinct C–O stretching bands at 1150 and 1260 cm^{-1} further confirm methacrylate network formation [28]. The appearance of bands at 1458 cm^{-1} and 1381 cm^{-1}, assigned to $–CH_2–$ scissoring and $–CH_3$ umbrella vibrations, respectively, provides direct evidence of a cross-linked polymer backbone. Notably, the presence of the $–CH_3$ band—absent in acrylamide—serves as a diagnostic marker for successful incorporation of EGDMA and confirms formation of a robust, three-dimensional imprinted matrix rather than linear polymer chains.

Following vanillin rebinding, the FTIR profile remains structurally consistent, indicating polymer stability. However, subtle band broadening and slight shifts in the O–H (~3400 cm^{-1}) and C=O (~1730 cm^{-1}) regions are observed, providing spectroscopic evidence of non-covalent hydrogen bonding between vanillin and the imprinted cavities. These interactions align with the proposed recognition mechanism and are later corroborated by DFT-calculated adsorption configurations.

3.1.5. XPS Analysis and Interfacial Electronic Structure

X-ray photoelectron spectroscopy (XPS) was employed to elucidate surface composition and electronic interactions. The survey spectrum of the bulk MIP (Fig.2b) shows only C, N, and O signals, with the N 1s peak at ~400 eV serving as a diagnostic signature of the acrylamide functional monomer. In contrast, the MIP/Co_3O_4/TiO_2 nanocomposite (Fig.2c) exhibits signals

View Article Online
DOI: 10.1039/D6AY00358C

corresponding to both polymer-derived elements (C 1s, N 1s) and core-derived metals (Co 2p and Ti 2p), confirming coexistence of the imprinted layer and electroactive inorganic core.

The Ti 2p spectrum displays a characteristic doublet at 458.5 eV (Ti $2p_{3/2}$) and 464.2 eV (Ti $2p_{1/2}$), which are positively shifted by ~0.26 eV relative to pristine TiO_2 [29]. Conversely, the Co 2p spectrum shows main peaks at 780.0 eV (Co $2p_{3/2}$) and 795.1 eV (Co $2p_{1/2}$), negatively shifted by ~0.4 eV compared to pure Co_3O_4 [30]. These opposing binding energy shifts provide compelling evidence of electron redistribution across the Co_3O_4/TiO_2 interface.

Specifically, electrons are transferred from n-type TiO_2 to p-type Co_3O_4 until Fermi level equilibration is achieved, resulting in the formation of an internal electric field at the p–n heterojunction [16,31]. This built-in field facilitates charge separation and accelerates interfacial electron transport, directly contributing to reduced charge-transfer resistance and enhanced electrochemical signal amplification. Importantly, the simultaneous detection of metal core signals beneath the polymer layer indicates that the MIP film is sufficiently thin and permeable, ensuring that molecular recognition does not compromise electronic communication with the electrode.

View Article Online
DOI: 10.1039/D6AY00358C

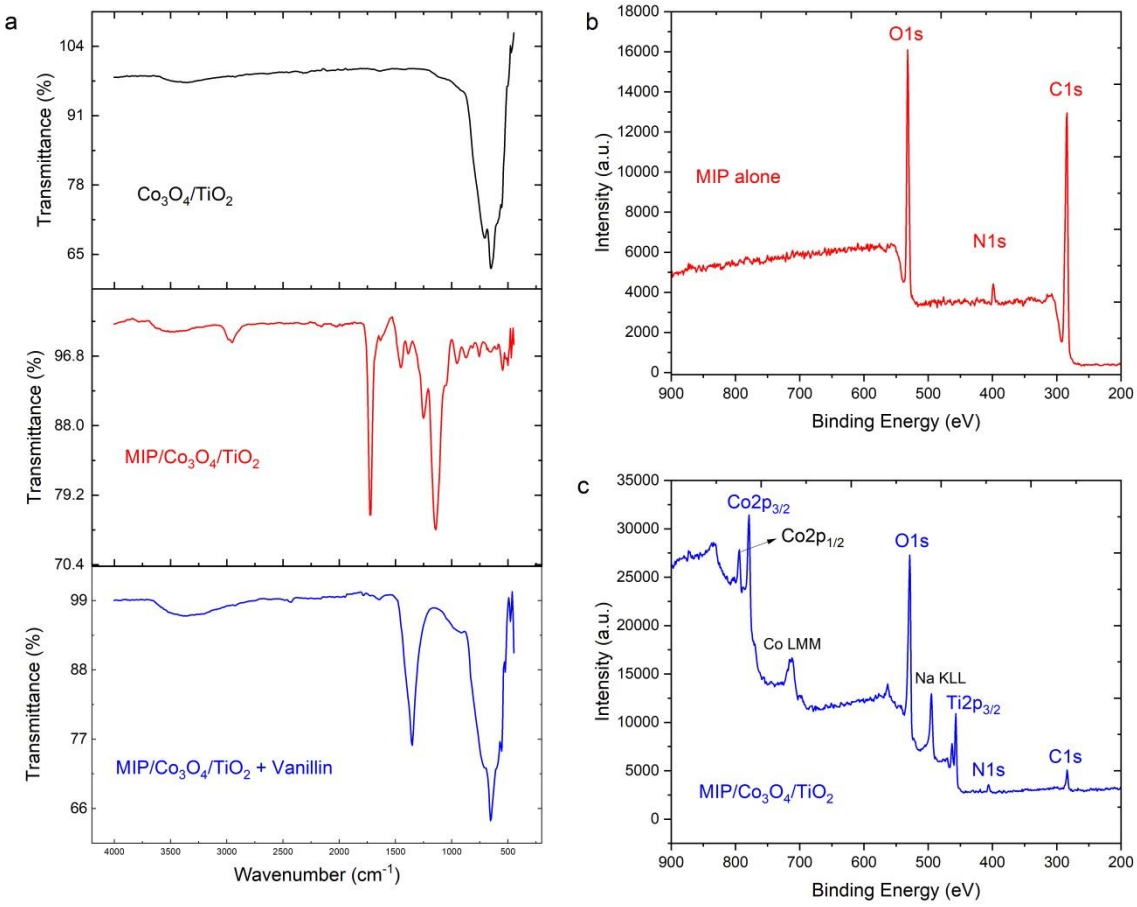

Fig. 2 a FTIR spectra of Co_3O_4/TiO_2, $MIP/Co_3O_4/TiO_2$, and vanillin-bound $MIP/Co_3O_4/TiO_2$ **b** XPS survey spectrum of MIP alone and **c** XPS survey spectrum of $MIP/Co_3O_4/TiO_2$

3.1.6. Mott-Schottky Analysis and p–n Heterojunction Band Alignment

While structural and elemental analyses indicate the physical integration of the metal oxides, the thermodynamic formation of the p–n heterojunction and its interfacial energetics were definitively mapped using Mott-Schottky (M-S) analysis. The interfacial capacitance (C) was measured as a function of applied potential (E) at 2.5 kHz, and the data were evaluated using the standard Mott-Schottky relation:

$$\frac{1}{C^2} = \frac{2}{\varepsilon\varepsilon_0 eNA^2}\left(E - E_{fb} - \frac{\kappa T}{e}\right)$$

View Article Online
DOI: 10.1039/D6AY00358C

where ε is the dielectric constant of the semiconductor, ε_0 is the vacuum permittivity, e is the elementary charge, N is the carrier density, A is the active area, and E_{fb} is the flat band potential. As shown in **Fig. 3a-d**, the pure oxide precursors exhibited archetypal single-semiconductor behavior. Pure Co_3O_4 displayed a negative slope, confirming holes as the majority charge carriers (p-type), with an extrapolated flat band potential (E_{fb}) of 0.108 V (vs. Ag/AgCl) and a high acceptor density ($N_A = 2.47\times10^{20}$ cm^{-3}). In contrast, pure TiO_2 yielded a positive slope characteristic of an n-type semiconductor, with an E_{fb} of 0.601 V and a donor density (N_D) of 2.33×10^{19} cm^{-3}.

Crucially, the M-S plot for the synthesized Co_3O_4/TiO_2 nanocomposite (**Fig.3e-f**) exhibited a distinct inverted "V" shape, featuring both negative and positive linear regions. This bipartite curve is the definitive electrochemical signature of a successfully formed p–n heterojunction. Upon intimate contact between the p-type Co_3O_4 and n-type TiO_2, the chemical potential gradient drives the diffusion of electrons from TiO_2 to Co_3O_4, and holes in the reverse direction, until the Fermi levels equilibrate. This equilibration fundamentally alters the localized band energetics. In the composite, the apparent flat band potentials shifted to 0.206 V for the p-region and 0.702 V for the n-region.

View Article Online
DOI: 10.1039/D6AY00358C

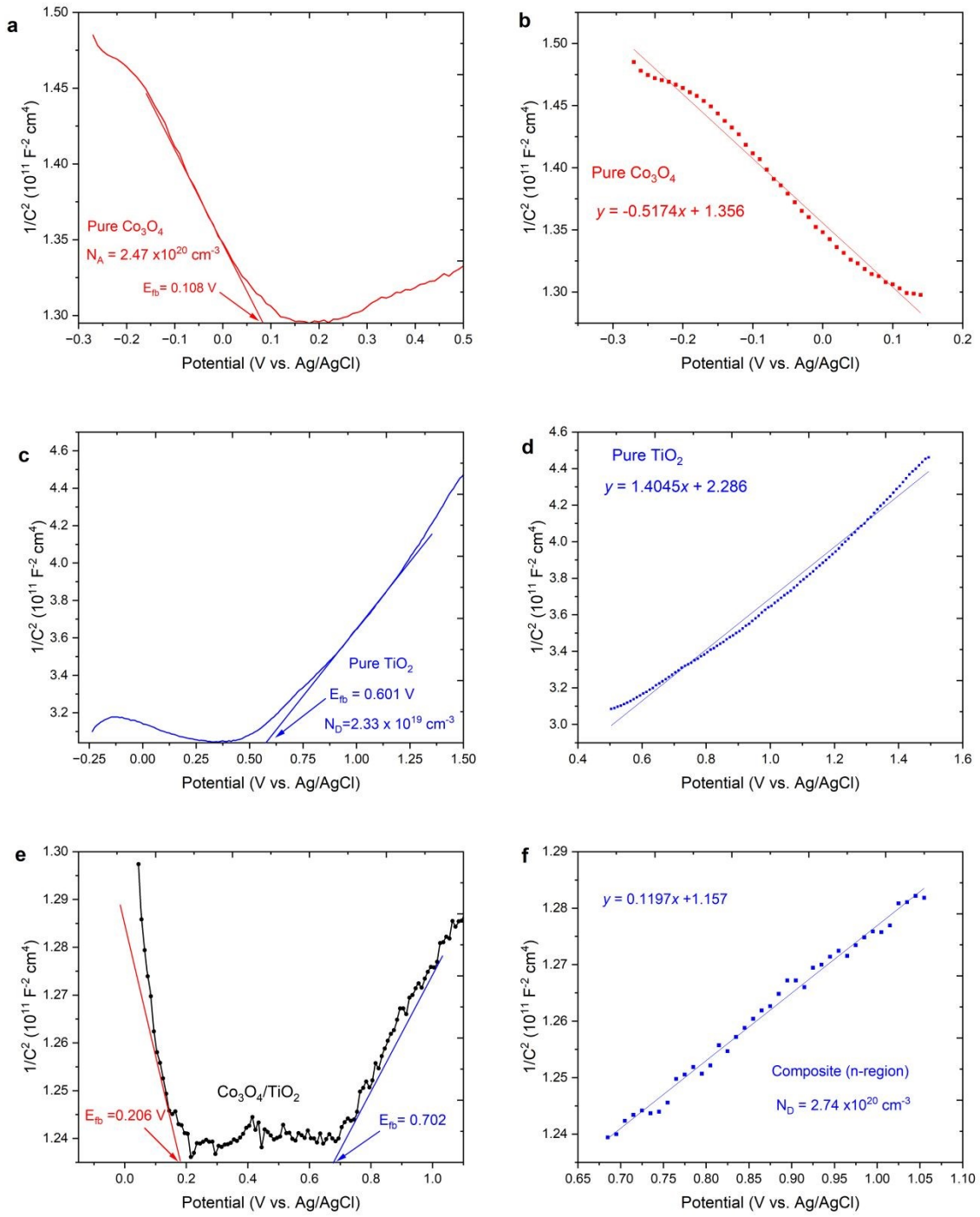

Fig.3. Mott-Schottky plots ($1/C^2$ vs. applied potential) demonstrating semiconductor type and interfacial band energetics. Measurements were performed for (**a, b**) pristine Co_3O_4 confirming p-type characteristics, (**c, d**) pristine TiO_2 confirming n-type characteristics, and (**e, f**) the Co_3O_4/TiO_2 nanocomposite. The bipartite, inverted "V" shape observed in the composite confirms the successful formation of a p–n heterojunction and enables the extraction of shifted flat band potentials (E_{fb}) to determine the built-in internal electric field.

View Article Online
DOI: 10.1039/D6AY00358C

The magnitude of the internal electric field generated at the depletion region—the built-in potential (V_{bi})—can be estimated from the difference between these shifted energy states. The calculated V_{bi} of 0.496 V establishes a powerful localized driving force that suppresses the recombination of electron-hole pairs. Consequently, during the electro-oxidation of vanillin, this built-in electric field rapidly sweeps electrons away from the catalytic interface, directly rationalizing the drastic reduction in charge-transfer resistance and the amplified anodic currents observed in the subsequent voltammetric studies.

3.2. Electrochemical Synergy and Interfacial Charge-Transfer Behavior

The electrochemical evolution of the sensing interface was quantitatively evaluated by cyclic voltammetry (CV) and electrochemical impedance spectroscopy (EIS) using the reversible $[Fe(CN)_6]^{3-/4-}$redox probe. These techniques provide complementary insight into surface conductivity, electroactive area, and interfacial charge-transfer kinetics at each fabrication stage.

Cyclic Voltammetry and Electroactive Surface Area

As shown in Fig.4a, the bare glassy carbon electrode (GCE) exhibited a pair of well-resolved redox peaks with an anodic peak current (I_{pa}) of 9.12 μA and a peak-to-peak separation (ΔE_p) of 64 mV, consistent with a quasi-reversible diffusion-controlled process. Upon modification with the Co_3O_4/TiO_2 nanocomposite, a dramatic enhancement in electrochemical activity was observed: the anodic current increased nearly 7.6-fold to 69.41 μA, while ΔE_p expanded to 350 mV. This behavior reflects rapid interfacial electron transport facilitated by the p–n heterojunction formed between p-type Co_3O_4 and n-type TiO_2, coupled with a substantial increase in electroactive surface area (ECSA) from 0.348 to 0.427 cm².

Following polymer deposition, distinct imprinting-dependent behavior emerged. The non-imprinted polymer (NIP) electrode showed severe current suppression (I_{pa} = 4.25 μA, ΔE_p = 401

View Article Online
DOI: 10.1039/D6AY00358C

mV), indicating that the dense polymer layer acts as an insulating barrier that blocks probe diffusion. In contrast, the MIP/Co_3O_4/TiO_2 electrode retained a high anodic current of 45.25 μA with a significantly narrower ΔE_p (166 mV), demonstrating that template removal generates accessible transport channels through the polymer matrix. The imprinting factor derived from CV was calculated as:

$$IF_{CV} = \frac{I_{pa}^{MIP}}{I_{pa}^{NIP}} = \frac{45.25}{4.25} \approx 10.6$$

This high IF_{CV} quantitatively confirms the formation of selective, electrochemically active imprinted cavities rather than nonspecific polymer porosity. Consistent with this trend, the electroactive surface area of the MIP electrode (0.303 cm²) remained substantially higher than that of the NIP, for which reliable ECSA estimation was not feasible due to signal attenuation.

Electrochemical Impedance Spectroscopy and Interfacial Kinetics

EIS measurements (**Fig.S3**) were fitted using a modified Randles equivalent circuit. This specific pattern was selected as it optimally models the physical phenomena at the porous electrode interface, incorporating uncompensated solution resistance (R_s), charge-transfer resistance (R_{ct}), and a constant phase element (CPE) to account for interfacial heterogeneity and non-ideal capacitance. The bare GCE exhibited a high R_{ct} of 4719 Ω·cm², reflecting intrinsically slow electron-transfer kinetics at the unmodified carbon surface. After Co_3O_4/TiO_2 deposition, R_{ct} decreased sharply to 17.9 Ω·cm², representing a >260-fold reduction. This drastic improvement directly evidences the electron-mediating role of the Co_3O_4/TiO_2 heterojunction, where Fermi level equilibration across the p–n interface establishes an internal electric field that accelerates charge transfer.

Introduction of the molecularly imprinted polymer resulted in a moderate increase in R_{ct} to 35.8 Ω·cm², attributable to the non-conductive polymer backbone [32]. Crucially, this value remains

View Article Online
DOI: 10.1039/D6AY00358C

over 130 times lower than that of the bare GCE, demonstrating that the imprinted cavities act as preferential electron-transfer conduits. By contrast, the NIP-modified electrode exhibited a higher resistance (43.3 Ω·cm²) and markedly inferior interfacial capacitance. The imprinting factor from EIS was quantified as:

$$IF_{EIS} = \frac{R_{ct}^{NIP}}{R_{ct}^{MIP}} = \frac{43.3}{35.8} \approx 1.21$$

Although the imprinting factor derived from EIS is intrinsically lower than that obtained from CV—owing to the sensitivity of impedance spectroscopy to the bulk dielectric and interfacial charge-transfer characteristics of the polymer layer—it nevertheless clearly evidences the enhanced charge-transfer accessibility of the imprinted architecture. This disparity is expected, as CV predominantly probes localized mass-transport and redox accessibility through imprint-generated pathways, whereas EIS integrates the overall interfacial response governed by polymer dielectric properties.

Validation of Imprinting Mechanism via Rebinding Studies

To definitively validate the fidelity and specific recognition capability of the imprinted cavities, stepwise electrochemical measurements were conducted on the MIP interface before and after template rebinding (**Fig.S4**). The unwashed MIP, wherein the cavities remain occupied by the vanillin template, exhibited heavily suppressed electrochemical activity characterized by a high R_{ct} (671.1 Ω·cm²) and low anodic current (11.38 μA cm⁻²). This confirms that the embedded target molecule acts as a physical barrier, sterically hindering the diffusion of the $[Fe(CN)_6]^{3-/4-}$ probe to the underlying electrocatalytic core. Upon complete elution of the template, the transport channels were unblocked, resulting in a sharp decrease in impedance (R_{ct} = 38.9 Ω·cm²) and a concurrent recovery of the anodic current (46.44 μA cm⁻²) presented in **Fig.S5**. Subsequently, when the eluted

View Article Online
DOI: 10.1039/D6AY00358C

electrode was re-incubated in a vanillin solution, the target molecules specifically reoccupied the tailored cavities. This successful rebinding once again blocked the probe pathways, causing the interfacial resistance to surge to 481.3 Ω·cm² and the current to drop to 13.45 μA cm⁻². This cyclical blocking and unblocking behavior provides unequivocal evidence of the successful formation of highly specific, dimensionally matched recognition sites within the polymer matrix.

Further mechanistic insight is provided by the double-layer capacitance (C_{dl}). The MIP electrode exhibited a C_{dl} of 18.0 μF, nearly three orders of magnitude larger than that of the NIP (0.01 μF). This striking contrast indicates that the NIP forms a thick dielectric barrier that suppresses interfacial polarization, whereas the MIP preserves electrolyte penetration and interfacial charge accumulation within the imprinted cavities. Collectively, the quantitative CV and EIS analyses demonstrate that the sensing interface benefits from a dual synergistic mechanism: (***i***) the Co_3O_4/TiO_2 p–n heterojunction dramatically enhances intrinsic electron-transfer kinetics and electroactive surface area, and (***ii***) molecular imprinting introduces selective, nanoscale transport channels that maintain electrochemical accessibility despite polymer encapsulation.

3.3. Electrochemical Recognition and Analytical Performance toward Vanillin

3.3.1. Electrochemical Behavior of Vanillin at the Modified Interfaces

The electrocatalytic oxidation of vanillin (50 μM, 0.1 M PBS, pH 7.0) was systematically investigated at the stepwise-modified electrodes using cyclic voltammetry (Fig.4b). Pronounced differences in oxidation kinetics and signal magnitude were observed, directly reflecting the interfacial architecture and recognition functionality.

At the bare GCE, vanillin produced a broad and weak anodic response with a peak current density of 3.84 μA cm⁻² at E_{pa} = 0.635 V, indicative of sluggish electron-transfer kinetics and poor

View Article Online
DOI: 10.1039/D6AY00358C

surface affinity typical of unmodified carbon electrodes. Upon modification with the Co_3O_4/TiO_2 heterojunction, the anodic peak current increased sharply to 51.86 μA cm^{-2}, corresponding to an approximately 13-fold enhancement. This substantial amplification arises from the synergistic coupling of p-type Co_3O_4 and n-type TiO_2, which promotes efficient interfacial charge separation, together with the presence of mixed-valence Co^{2+}/Co^{3+} redox centers that facilitate catalytic oxidation of the phenolic hydroxyl group in vanillin.

Notably, the MIP/Co_3O_4/TiO_2/GCE delivered the highest current response (70.03 μA cm^{-2} at E_{pa} = 0.655 V), representing an ~18-fold enhancement relative to the bare electrode. This behavior contrasts with the attenuation observed for the outer-sphere $[Fe(CN)_6]^{3-/4-}$ probe, where the polymer layer partially hindered electron transfer. In the presence of vanillin, however, the imprinted polymer acts as an analyte-specific accumulation layer, selectively capturing and pre-concentrating vanillin within geometrically and chemically complementary cavities. This local enrichment at the electrode–electrolyte interface effectively compensates for the insulating nature of the polymer matrix and maximizes access to the underlying catalytic heterojunction. The result confirms that the sensing interface integrates molecular recognition and electrocatalysis in a cooperative manner, yielding a response unattainable by either component alone.

3.3.2. Influence of Solution pH and Reaction Mechanism

The pH of the supporting electrolyte critically governs both the oxidation kinetics and the interfacial recognition of vanillin. The electrochemical response of the MIP/Co_3O_4/TiO_2 sensor was therefore evaluated over a pH range of 5.0–9.0 (Fig. 4c).

Effect on Peak Current (Ipa): The anodic peak current exhibited a pronounced dependence on solution pH, reaching a maximum of 54.82 μA cm^{-2} at pH 7.0**.** Slightly lower currents were observed at pH 5–6, while a marked decrease occurred under alkaline conditions, dropping to

View Article Online
DOI: 10.1039/D6AY00358C

42.92 μA cm^{-2} (pH 8.0) **and** 36.54 μA cm^{-2} (pH 9.0)**.** This trend reflects the acid–base behavior of vanillin (pKa ≈ 7.4). At neutral pH, vanillin exists predominantly in its molecular form, favoring hydrogen bonding and π–π interactions within the imprinted cavities. At pH values above the pKa, deprotonation yields phenolate anions, while concurrent deprotonation of surface hydroxyl groups ($M–O^-$) and polymer functionalities imparts a net negative surface charge. The resulting electrostatic repulsion suppresses analyte uptake into the recognition sites, leading to diminished current response.

Effect on Peak Potential (E_{pa}) and Mechanistic Insight: As shown in Fig. S6a, the oxidation peak potential shifted linearly toward more negative values with increasing pH, following the relationship:

$$E_{pa}(V) = -0.0495\,pH + 0.8579 \quad (R^2 = 0.9969)$$

The slope of 49.5 mV pH^{-1} is close to the theoretical Nernstian value (59 mV pH^{-1} at 25 °C), indicating that the number of protons involved in the rate-determining step is approximately equal to the number of transferred electrons (m ≈ n). This behavior is consistent with a $1e^-/1H^+$ oxidation mechanism**,** where vanillin undergoes proton-coupled electron transfer to form a phenoxy radical intermediate, followed by further chemical stabilization or coupling. Based on both maximal signal intensity and mechanistic stability, pH 7.0 was selected as the optimal electrolyte for all subsequent analytical evaluations.

View Article Online
DOI: 10.1039/D6AY00358C

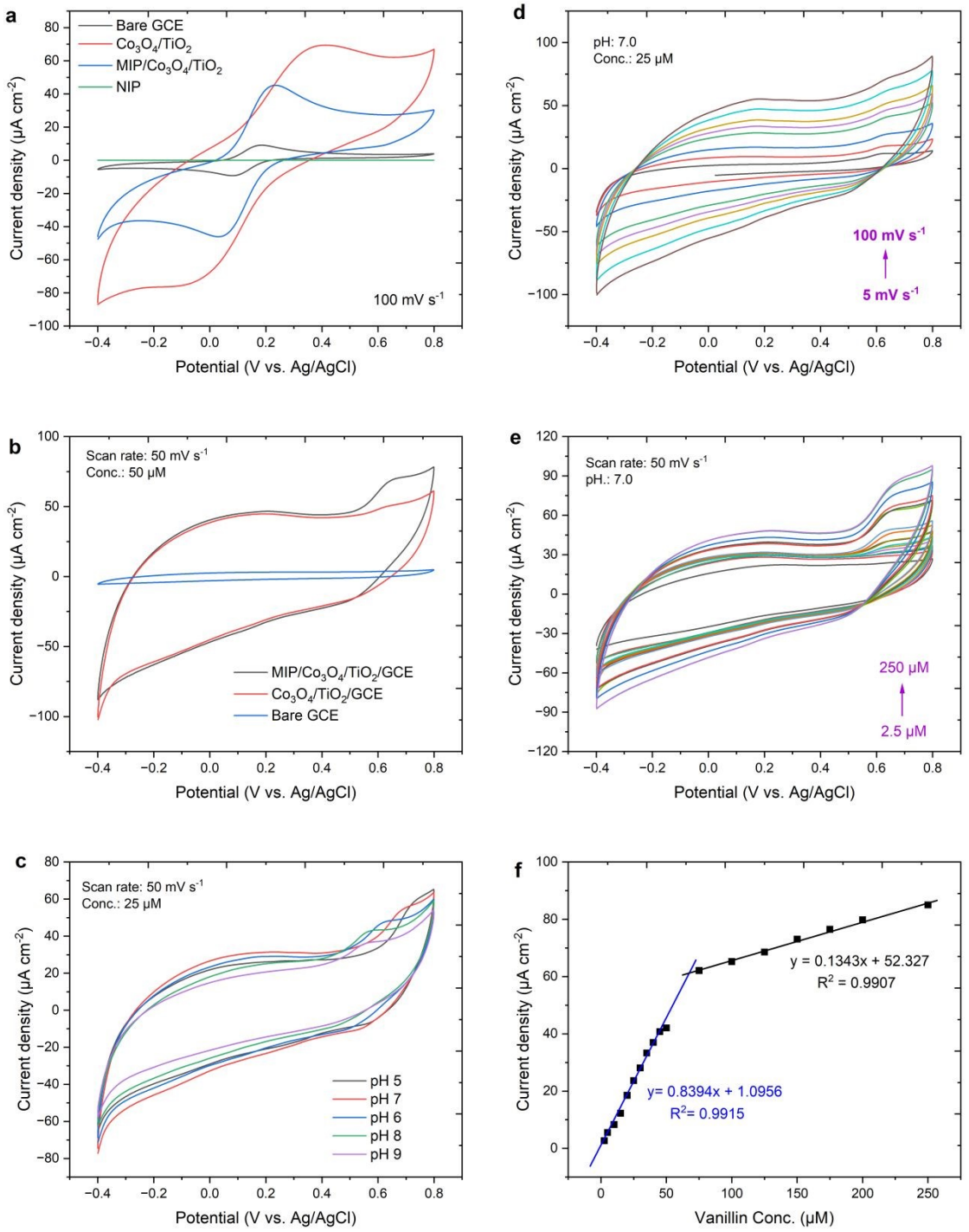

Fig.4: **a** CVs of bare GCE and modified GCE in 2 mM $[Fe(CN)_6]^{3-/4-}$ **b** CVs of bare GCE and modified GCE in vanillin **c** Effect of solution pH on the anodic peak current **d** CVs at different scan rates **e** Variation in vanillin concentration **f** Calibration curves for vanillin determination showing two linear concentration ranges.

View Article Online
DOI: 10.1039/D6AY00358C

3.3.3. Optimization of Polymer Layer Thickness and Mass Transport

The thickness and cross-linking density of the MIP layer are critical parameters that dictate the balance between specific recognition capacity and the kinetic efficiency of analyte diffusion. To prevent the formation of an excessively thick polymer shell that could insulate the electrocatalytic core, the thermal polymerization time was systematically optimized (**Fig.5**). The anodic peak current for 25 μM vanillin exhibited a pronounced dependency on polymerization duration. At 12 h and 18 h, the structural framework of the polymer was under-evolved, leading to an insufficient density of imprinted cavities and correspondingly low current responses (22.58 and 45.22 μA cm^{-2}, respectively). The maximum electrocatalytic response (54.82 μA cm^{-2}) was achieved at 24 h, indicating the formation of a robust, highly populated recognition layer that remained sufficiently permeable to facilitate rapid mass transport. Conversely, extending the polymerization to 36 h resulted in a significant signal suppression (36.58 μA cm^{-2}). This decline confirms that excessive polymerization yields an overly thick, dense dielectric barrier that severely restricts the diffusional pathways of vanillin to the internal Co_3O_4/TiO_2 heterojunction. Consequently, 24 h was established as the optimal polymerization time to maximize sensitivity.

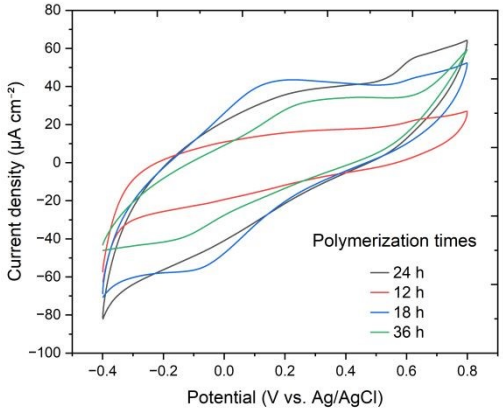

Fig.5. Optimization of the MIP layer thickness and mass transport kinetics. Cyclic voltammograms demonstrating the effect of thermal polymerization time (12, 18, 24, and 36 h) on the electrocatalytic oxidation of 25 μM vanillin. The signal peak at 24 h represents the optimal equilibrium between imprinted cavity density and polymer shell permeability.

View Article Online
DOI: 10.1039/D6AY00358C

3.3.4. Scan Rate Dependence and Mass-Transport Regime

To elucidate the kinetics and transport mechanism governing vanillin oxidation, cyclic voltammograms were recorded at scan rates ranging from 5 to 100 mV s^{-1} for 25 μM vanillin (Fig. 4d). The anodic peak current increased monotonically with scan rate, accompanied by a slight positive shift in peak potential (from 0.625 V at 5 mV s^{-1} to 0.657 V at 100 mV s^{-1}), confirming the irreversible nature of the oxidation process. Analysis of the current–scan rate relationship revealed that the dependence of I_{pa} on the square root of scan rate provided superior linearity (Fig.S6b):

$$I_{pa} = 7.694\, v^{1/2} - 6.579 \quad (R^2 = 0.9973)$$

compared with the linear I_{pa}–ν relationship (R^2 = 0.9835) (Fig.S6c). This clearly indicates that the oxidation of vanillin at the MIP/Co_3O_4/TiO_2 interface is predominantly diffusion-controlled. Mechanistically, this implies that adsorption into the imprinted cavities is rapid and not rate-limiting, while the overall current is governed by the diffusion of vanillin molecules through the porous polymer network to the electrocatalytic heterojunction. This behavior aligns with SEM observations of a coral-like, interconnected morphology that supports efficient mass transport while minimizing surface fouling.

3.3.5. Calibration Characteristics and Detection Capability

The quantitative sensing performance was evaluated by recording the CV response of the MIP/Co_3O_4/TiO_2 electrode to increasing vanillin concentrations (2.5–250 μM) in PBS (pH 7.0) (Fig. 4e). The anodic peak current at ~0.635 V increased systematically with concentration, yielding a calibration plot with two distinct linear regions (Fig. 4f).

Region I (2.5–75 μM): High-affinity recognition: A steep slope of 0.8394 μA μM^{-1} cm^{-2} (R^2 = 0.9915) was obtained, corresponding to selective occupancy of high-affinity imprinted cavities

View Article Online
DOI: 10.1039/D6AY00358C

located at or near the polymer surface. These sites provide optimal geometric and chemical complementarity, resulting in rapid accumulation and efficient electron transfer.

Region II (75–250 μM): Saturation-controlled response: At higher concentrations, the sensitivity decreased to 0.1343 μA μM^{-1} cm^{-2} (R^2 = 0.9907), reflecting saturation of specific cavities and a transition toward diffusion to lower-affinity or non-specific sites. Despite the reduced slope, excellent linearity was maintained, extending the dynamic range well beyond concentrations typically encountered in food products. The limits of detection and quantification were calculated using the standard deviation of the blank response (σ = 0.017 μA cm^{-2}, $n = 5$) and the slope of the high-sensitivity region:

- LOD = 0.06 μM
- LOQ = 0.20 μM

These values are substantially lower than vanillin levels commonly found in commercial foods (≈60–3000 μM), confirming that the sensor is well suited for direct analysis of complex food matrices without extensive preconcentration.

Due to the biphasic nature of the calibration curve, the sensor exhibits maximum analytical reliability and a 6.3-fold higher sensitivity within the primary linear range (2.5–75 μM), corresponding to the selective occupation of high-affinity imprinted cavities. Because commercial food products and flavoring extracts frequently contain endogenous vanillin concentrations exceeding this threshold, strict sample dilution protocols were employed to ensure regulatory compliance and quantification accuracy. Prior to electrochemical analysis, food sample extracts were diluted using the supporting electrolyte to ensure the working analyte concentration fell securely within the highly sensitive primary linear region (<75 μM). The endogenous vanillin concentration of the original matrix was subsequently determined by back-calculating with the

View Article Online
DOI: 10.1039/D6AY00358C

applied dilution factor, thereby circumventing the risk of signal underestimation associated with cavity saturation at higher concentrations.

3.4. Selectivity and Interference Studies

Selectivity is the defining performance metric of molecularly imprinted electrochemical sensors. The discrimination capability of the MIP/Co_3O_4/TiO_2 electrode was evaluated by recording the CV response of 25 μM vanillin in the presence of representative inorganic ions and organic matrix components commonly encountered in food samples (Fig. 6a).

Single-Component Interference: As shown in Fig. 6a, the addition of K^+, Na^+, Mg^{2+}, Ca^{2+}, and common saccharides (glucose, fructose, sucrose) at equimolar concentrations induced negligible variations in anodic peak current ($\Delta I/I_0$ = −3.7% to +2.3%). These results confirm that the imprinted recognition sites selectively accommodate vanillin through complementary size, geometry, and hydrogen-bonding interactions, while sterically and chemically mismatched species are effectively excluded [33].

Structural Analogs and Flavor Additives: To directly address the sensor's capability to discriminate against structurally similar compounds that often coexist in flavoring formulations, the sensor was challenged with benzaldehyde (a ubiquitous aldehyde flavorant) and 2,4,5-trichlorophenol (a representative phenolic analog) (**Fig.S7**). At equimolar ratios (1:1), the introduction of benzaldehyde and 2,4,5-trichlorophenol resulted in negligible signal changes of -3.36% and +0.51%, respectively. To rigorously test the boundaries of this selectivity, massive excess concentrations were applied. Even in the presence of a 100-fold excess of 2,4,5-trichlorophenol, the signal deviation was only -3.14%. Most remarkably, exposing the sensor to a 4000-fold excess of benzaldehyde (0.1 M) resulted in a modest signal suppression of just 11.71%. This robust discrimination confirms that molecules lacking the exact functional group arrangement

View Article Online
DOI: 10.1039/D6AY00358C

(e.g., benzaldehyde lacking specific –OH and $–OCH_3$ anchoring points) or possessing mismatched steric bulk (e.g., chlorinated phenols) cannot favorably coordinate within the specific imprinted cavities.

Multi-Component Matrix Challenge: To simulate realistic food matrices, mixed interferent systems containing 50-fold and 75-fold excess concentrations were examined (Fig. 6b). Under these aggressive conditions, the sensor preserved a stable response in the range of 53.8–56.8 μA cm^{-2}, indicating excellent resistance to competitive adsorption. Moderate signal suppression (13–18%) was observed only in mixtures containing citric acid and sucrose, which is attributed to partial pore blockage arising from non-specific physisorption. Importantly, even under these conditions, >80% signal retention was maintained, confirming the robustness of the imprinting strategy.

Ascorbic Acid Interference: A pronounced current enhancement was observed in the presence of ascorbic acid (AA) (Fig. 6c). This behavior arises from the intrinsic electroactivity of AA, which undergoes oxidation within a similar potential window on transition metal oxide surfaces [34]. Due to its small molecular size, AA can permeate the MIP layer and access the Co_3O_4/TiO_2 catalytic sites, leading to overlapping faradaic contributions. Accordingly, for vitamin C–rich samples, dilution or enzymatic pretreatment is required to ensure analytical accuracy.

3.5.Reproducibility and Fabrication Consistency

Fabrication reproducibility was assessed using six independently prepared MIP/Co_3O_4/TiO_2 electrodes under identical conditions (25 μM vanillin, 50 mV s^{-1}). As shown in Fig. 6d, the voltammograms exhibit excellent overlap, with invariant oxidation potentials and closely clustered current responses. The recorded anodic peak current densities were 58.95, 57.34, 56.83, 56.97, 54.30, and 53.96 μA cm^{-2}, corresponding to a relative standard deviation (RSD) of 3.39% (n = 6).

View Article Online
DOI: 10.1039/D6AY00358C

This low variability demonstrates that the hydrothermal deposition and electropolymerization processes yield a highly uniform interfacial architecture, satisfying reproducibility requirements for analytical deployment.

3.6.Long-Term Stability and Storage Performance

The operational stability of the sensor was evaluated over 42 days under two storage conditions: room temperature (25 ± 1 °C) and refrigerated storage (10 ± 1 °C).

Room Temperature Storage: As shown in Fig. 6e, the sensor retained 97.6% of its initial response after 15 days, followed by a gradual decline to 75.3% by Day 42. This degradation is attributed to slow polymer chain relaxation and progressive surface oxidation of the metal oxide active sites.

Refrigerated Storage: In contrast, refrigerated storage significantly mitigated signal loss (Fig. 6f). The electrode preserved 94.2% of its initial response after 30 days and 89.8% after 42 days, demonstrating effective stabilization of both the imprinted polymer network and the Co_3O_4/TiO_2 heterojunction. These results confirm that, when stored under mild refrigeration, the MIP/Co_3O_4/TiO_2 sensor maintains reliable analytical performance for over six weeks, meeting practical requirements for routine food quality control and laboratory analysis. By integrating molecular imprinting–driven chemical selectivity with a Co_3O_4/TiO_2 heterojunction that promotes fast, diffusion-controlled electron transfer, this platform delivers sub-micromolar vanillin detection with high matrix tolerance and operational stability, positioning it as a practical electroanalytical tool for routine food quality control without extensive sample pretreatment.

View Article Online
DOI: 10.1039/D6AY00358C

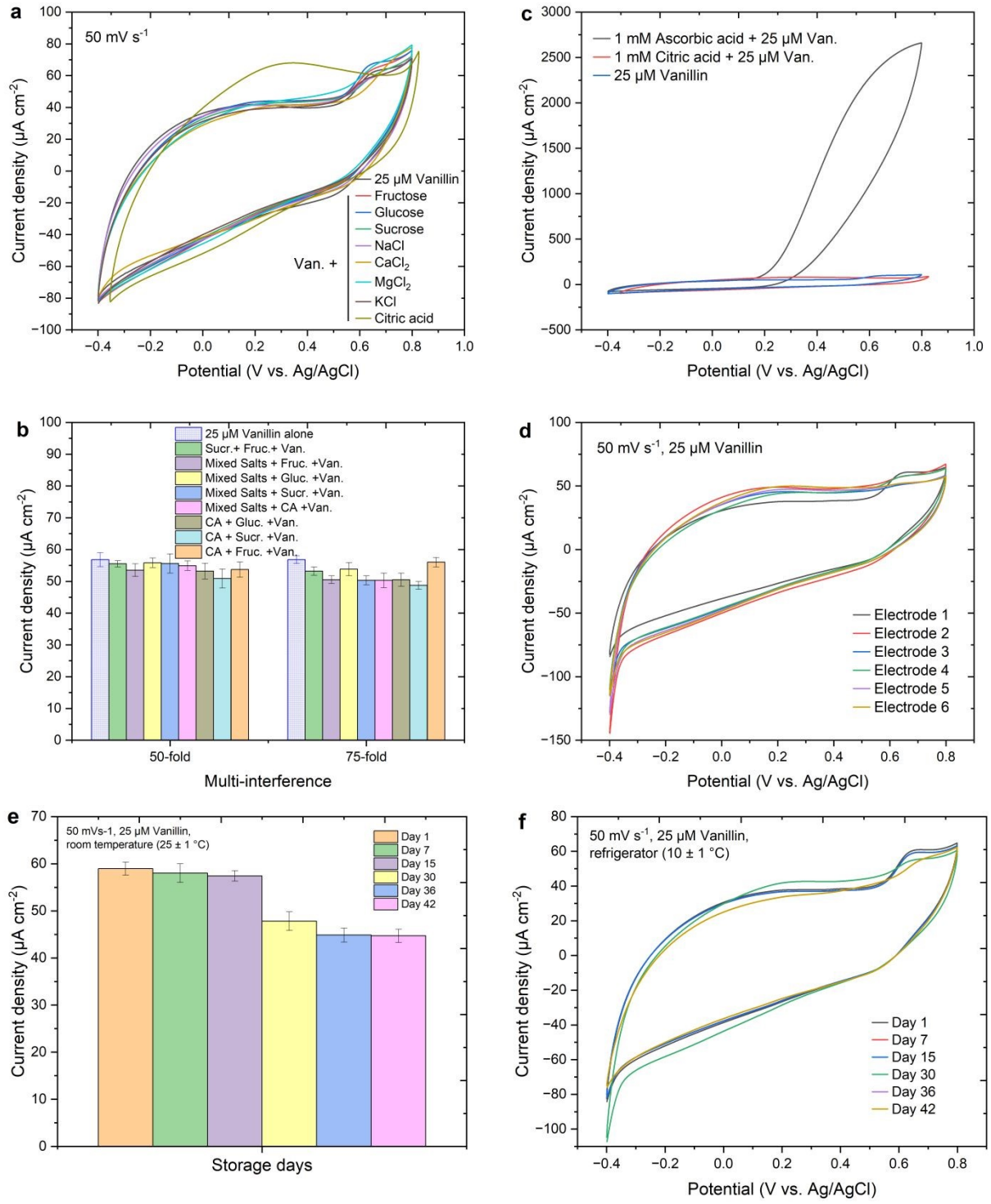

Fig.6: **a** Single-component interference **b** Multi-component matrix effect **c** Ascorbic acid interference **d** Reproducibility measurements **e** Stability studies in room temperature **f** Stability studies in refrigerated storage

View Article Online
DOI: 10.1039/D6AY00358C

3.7. Antifouling Capabilities and Matrix Stability

In continuous electrochemical monitoring of food products, the accumulation of macromolecules (e.g., proteins, lipids) and phenolic compounds often leads to severe electrode passivation, a phenomenon known as cumulative fouling. To rigorously evaluate the antifouling properties of the MIP/Co_3O_4/TiO_2 architecture, the sensor was subjected to repetitive cyclic voltammetry (50 continuous cycles) directly in unspiked, pretreated milk and coffee matrices, serving as models for high-protein/lipid and polyphenol-rich environments, respectively (**Fig.7**).

The evolution of the voltammetric profiles reveals distinct, matrix-dependent interfacial dynamics. In the milk matrix (**Fig. 7a-b**), a slight, gradual suppression of the capacitive background current was observed (from 41.83 to 31.22 μA cm^{-2} over 50 cycles). This stabilization indicates minor adsorption of denatured proteins or lipid aggregates onto the outer polymer surface, which mildly reduces the interfacial double-layer capacitance. Conversely, in the coffee matrix (**Fig. 7c-d**), the capacitive background current exhibited a steady increase from 66.01 to 82.53 μA cm^{-2}. This behavior is characteristic of the non-specific adsorption of electroactive polyphenolic compounds, which accumulate on the exterior of the polymer network and undergo continuous redox cycling, thereby elevating the total interfacial charge.

Crucially, the integrity of the vanillin recognition mechanism was preserved in both aggressive environments. To quantify the extent of cumulative passivation, the sensor's response to a standard 25 μM vanillin solution in PBS was measured before and immediately after the 50-cycle matrix exposure (**Fig. 7f**). The sensor exposed to the milk matrix exhibited an anodic peak current of 49.11 μA cm^{-2}, translating to an excellent signal retention of 89.58% (a sensitivity loss of merely 0.21% per cycle). Remarkably, the sensor exposed to the coffee matrix retained 97.90% of its original response (53.67 μA cm^{-2}), despite the heavy outer accumulation of polyphenols.

View Article Online
DOI: 10.1039/D6AY00358C

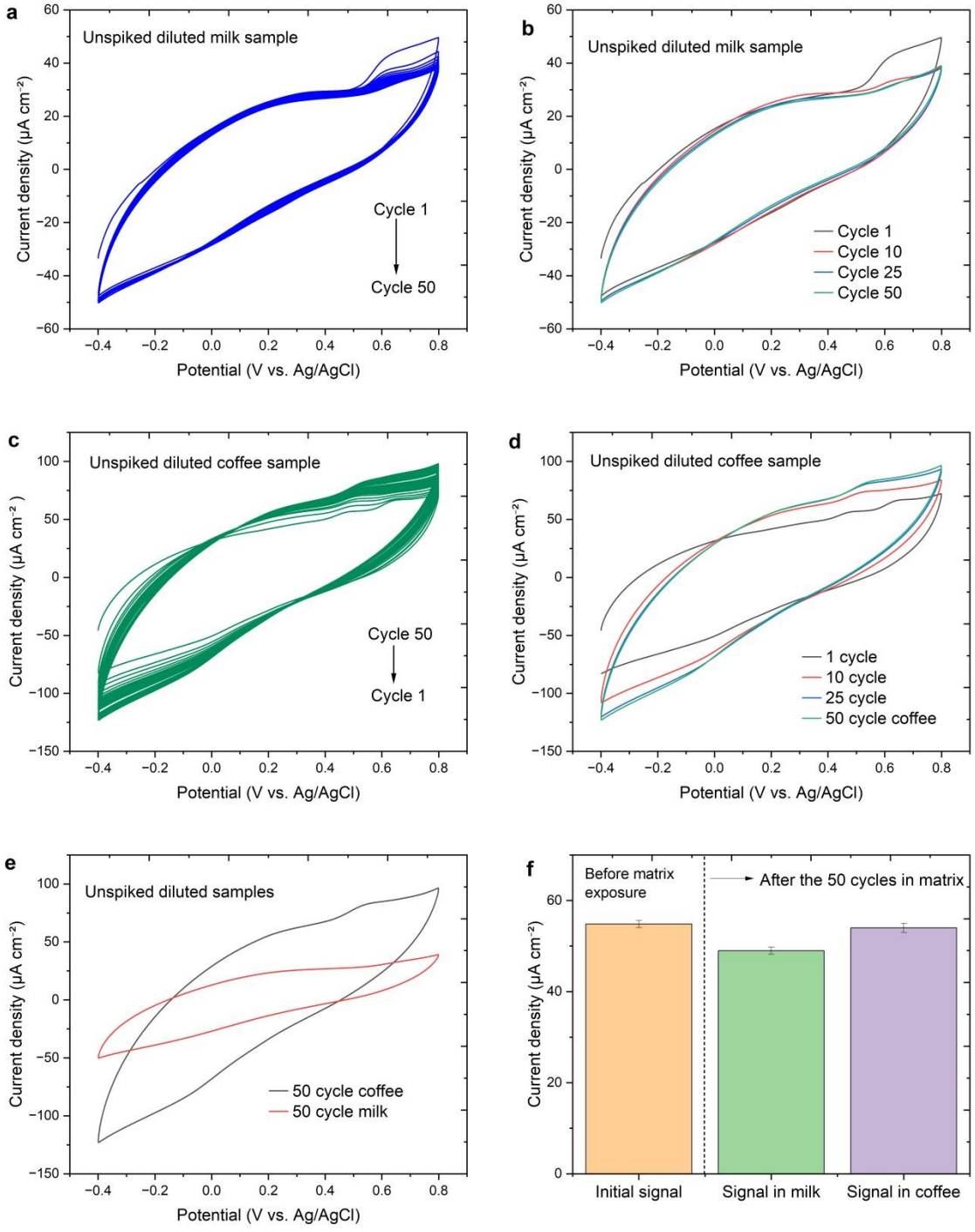

Fig.7: Antifouling performance and matrix stability of the MIP/Co_3O_4/TiO_2 sensor. Continuous cyclic voltammograms (50 cycles) recorded in unspiked (**a, b**) milk and (**c, d**) coffee matrices. (**e**) Overlay comparison of the 50th CV cycle in both matrices. (**f**) Anodic peak current response for 25 μM vanillin before (initial) and after the 50-cycle exposure to the respective food matrices, demonstrating high signal retention.

View Article Online
DOI: 10.1039/D6AY00358C

These findings confirm that the molecularly imprinted layer functions as a highly robust, permselective shield. While matrix interferents may dynamically interact with the macroscopic surface, they are sterically and chemically excluded from penetrating the customized imprinted cavities. Consequently, the internal heterojunction catalytic sites remain unobstructed, ensuring high-fidelity quantification of vanillin without the need for extensive sample cleanup or continuous electrode renewal.

3.8. Real Sample Analysis and Method Validation

The practical applicability of the proposed MIP/Co_3O_4/TiO_2 electrochemical sensor was rigorously evaluated through the determination of vanillin in five commercially available food products representing a broad spectrum of matrix complexity, including lipid- and protein-rich dairy products (milk and ice cream), carbohydrate-dense solid foods (biscuits), and polyphenol-containing beverages (coffee and iced tea). These matrices are analytically challenging due to their high fouling propensity, coexisting electroactive species, and variable physicochemical compositions, providing a stringent test of sensor robustness [34–38].

Quantification of Endogenous Vanillin: As summarized in Table 1, the sensor enabled direct quantification of endogenous vanillin in flavored products without extensive sample pretreatment. Vanillin concentrations of 452.1 μM (milk), 118.4 μM (ice cream), and 142.7 μM (biscuits) were reliably determined, falling well within the typical concentration ranges reported for commercial food formulations. In contrast, no discernible oxidation peaks attributable to vanillin were observed in unflavored coffee and iced tea samples ("ND"), confirming the absence of false-positive responses arising from matrix-derived phenolics, caffeine, or organic acids. This result highlights the high chemical selectivity imparted by the molecularly imprinted polymer layer, even in chemically complex beverage matrices [39].

View Article Online
DOI: 10.1039/D6AY00358C

Accuracy and Recovery Performance: Method accuracy was assessed via standard addition recovery experiments using three spiking levels (25, 50, and 75 μM vanillin). Across all matrices, the sensor exhibited excellent recovery values ranging from 96.8% to 103.2%, with relative standard deviations (RSDs) consistently below 4.0% (n = 4). These results demonstrate that the porous MIP architecture effectively mitigates electrode fouling and matrix suppression effects, enabling reproducible analyte access to the electrocatalytic Co_3O_4/TiO_2 heterojunction. Notably, even in high-fat and protein-rich dairy samples—conditions that typically compromise electrochemical interfaces—the sensor maintained quantitative accuracy, underscoring the perm-selective and antifouling nature of the imprinted polymer layer.

Validation against Reference Methods: To benchmark analytical reliability, the electrochemical results were systematically compared with established reference techniques, namely high-performance liquid chromatography (HPLC) and UV–Vis spectrophotometry (Table 1). The proposed sensor showed excellent agreement with both methods, with relative errors (RE) consistently below 4.0% for all quantified samples. For milk, the deviation from HPLC was only 0.94%, demonstrating near-equivalence to chromatographic analysis. In the case of coffee, HPLC detected a trace vanillin concentration (0.28 μM), which lies near the instrumental quantification limit and is statistically consistent with the "ND" classification obtained electrochemically. This minor discrepancy reflects the fundamentally different detection principles of chromatographic versus electrochemical methods and does not indicate analytical bias. Importantly, the electrochemical sensor achieves comparable accuracy while offering substantial advantages in terms of analysis time, operational simplicity, cost, and portability.

Overall, these validation results confirm that the MIP/Co_3O_4/TiO_2 sensor provides reliable, matrix-tolerant quantification of vanillin in real food samples, meeting the analytical performance

View Article Online
DOI: 10.1039/D6AY00358C

criteria required for routine quality control and on-site screening applications. The validated concentration range and low detection limit of the proposed MIP/Co_3O_4/TiO_2 sensor comfortably encompass the vanillin levels specified in international food labeling and additive regulations, enabling rapid verification of declared flavor content. This positions the platform as a practical screening tool for routine regulatory compliance, adulteration detection, and quality assurance in food manufacturing and inspection settings.

Table 1: Quantification of vanillin in food samples by the MIP/Co_3O_4/TiO_2 sensor with recovery and method comparison (HPLC, UV–Vis).

Sample	Original Found (µM)	Added (µM)	Total Found (µM)	Recovery (%)	RSD (%)
Milk	452.1	25.0	476.5 (±0.039)	97.6	2.15
		50.0	503.2 (±0.012)	102.2	2.40
		75.0	525.8 (±0.021)	98.3	2.65
Ice Cream	118.4	25.0	144.2 (±0.013)	103.2	3.12
		50.0	169.1 (±0.011)	101.4	2.85
		75.0	192.5 (±0.025)	98.8	3.05
Biscuits	142.7	25.0	166.9 (±0.016)	96.8	2.94
		50.0	193.5 (±0.028)	101.6	3.05
		75.0	218.4 (±0.031)	100.9	3.20
Coffee	ND	25.0	24.8 (±0.028)	99.2	3.55
		50.0	51.4 (±0.033)	102.8	3.10
		75.0	74.1 (±0.027)	98.8	3.45
Iced Tea	ND	25.0	25.6 (±0.025)	102.4	3.80
		50.0	48.9 (±0.015)	97.8	3.65
		75.0	73.5 (±0.012)	98.0	3.90

Sample	Sensor (µM)	HPLC (µM)	UV-Vis (µM)	RE vs. HPLC (%)	RE vs. UV-Vis (%)
Milk	452.1	447.9	457.3	**0.94**	1.14
Ice Cream	118.4	115.5	117.8	2.51	0.51
Biscuits	142.7	145.5	148.5	1.92	3.91
Coffee	ND	0.28	ND	—	—
Iced Tea	ND	ND	ND	—	—

ND: Not Detected (< LOD); Tabulated results are based on n =4 ± standard deviation; Statistical comparison using paired t-test and F-test at the 95% confidence level showed no significant difference between the proposed sensor and reference methods ($p > 0.05$); detailed statistical analysis is provided in Section S2.2.

View Article Online
DOI: 10.1039/D6AY00358C

3.9. DFT-Supported Sensing Mechanism

To elucidate the molecular origin of selectivity and signal amplification in the MIP/Co_3O_4/TiO_2 sensor, density functional theory (DFT) calculations coupled with Monte Carlo adsorption simulations were employed. As depicted in **Scheme 1**, vanillin interacts with acrylamide through directional hydrogen bonding during the pre-polymerization stage, leading to the formation of spatially and chemically complementary recognition sites upon template removal. Accordingly, the computational framework was designed to (i) determine the optimal vanillin–monomer stoichiometry governing cavity fidelity, (ii) quantify adsorption energetics and interaction hierarchies for vanillin relative to structurally relevant interferents, and (iii) mechanistically link molecular-level recognition events to experimentally observed electrochemical responses, including charge-transfer resistance modulation and sensitivity enhancement.

3.9.1. Model Construction and Computational Methodology

The molecularly imprinted environment was modeled using acrylamide as the functional monomer, selected for its strong hydrogen-bond donor/acceptor capability toward phenolic and aldehydic functionalities. Vanillin, glucose, and ascorbic acid were treated as template or competing analytes to reflect the experimental selectivity landscape. For vanillin–acrylamide assemblies, four stoichiometric ratios (1:1, 1:2, 1:3, and 1:4) were evaluated to capture cooperative binding effects. Initial adsorption configurations were generated using the Adsorption Locator module with simulated annealing under the COMPASSIII force field, allowing full translational, rotational, and regrowth freedom of the monomers. The lowest-energy adsorption poses were subsequently refined via DFT geometry optimization using the DMol³ module. Interaction energies (ΔE) were calculated according to:

$$\Delta E = E_{complex} - \left(E_{template} + n \times E_{monomer}\right)$$

View Article Online
DOI: 10.1039/D6AY00358C

where negative ΔE values indicate thermodynamically favorable complex formation. This combined Monte Carlo–DFT strategy ensures both global conformational sampling and accurate electronic-level interaction analysis, consistent with MCA computational standards.

3.9.2. Binding Stoichiometry and Energetic Optimization

The calculated interaction energies for vanillin–acrylamide complexes reveal a pronounced dependence on monomer stoichiometry. As summarized below, the binding strength increases sharply from 1:1 to 1:3, followed by a decline at higher monomer loading:

- **1:1**: −0.18 kcal mol^{-1} (very weak, insufficient interaction sites)
- **1:2**: −13.36 kcal mol^{-1} (strong, partial hydrogen-bond network)
- **1:3**: **−28.49 kcal mol^{-1} (very strong, optimal cooperative binding)**
- **1:4**: −12.66 kcal mol^{-1} (weakened due to steric crowding)

The 1:3 vanillin:acrylamide ratio clearly represents the thermodynamic optimum, where three acrylamide units cooperatively engage vanillin through multiple hydrogen bonds without introducing steric frustration. This result (see Table S1) provides molecular-level justification for the experimentally observed high imprinting efficiency and validates the monomer composition employed during polymer synthesis.

3.9.3. Adsorption Configuration and Origin of Selectivity

The lowest-energy adsorption configuration for the vanillin–acrylamide (1:3) assembly (**Fig.8**) reveals a highly ordered, multipoint recognition motif consistent with the imprinting mechanism illustrated in **Scheme 1**. In this optimized geometry, vanillin is anchored within the cavity through cooperative hydrogen bonding between its phenolic –OH and aldehydic –CHO groups and the –NH/–C=O functionalities of acrylamide, yielding a total system energy of −225.67 kcal mol^{-1} and an isosteric heat of adsorption of 16.19 kcal mol^{-1}. The low deformation energy (≈ −6 kcal mol^{-1})

View Article Online
DOI: 10.1039/D6AY00358C

confirms that binding occurs without significant structural distortion, indicating excellent geometric and chemical complementarity between the template and the imprinted sites formed after polymerization and template removal (Scheme 1).

In contrast, common interferents exhibit markedly weaker and less cooperative adsorption behavior. The glucose–acrylamide (1:3) assembly shows a much lower interaction energy (−12.57 kcal mol^{-1}), dominated by non-directional hydrogen bonding from multiple hydroxyl groups, resulting in poor confinement and reduced stabilization (average total system energy: −224.96 kcal mol^{-1}). Ascorbic acid displays intermediate affinity (−20.23 kcal mol^{-1}), attributed to its enediol functionality, but lacks the rigid aromatic framework required to achieve cavity matching comparable to vanillin. These energetic and structural differences establish the selectivity hierarchy:

$$Vanillin \gg Ascorbic\ Acid > Glucose$$

which directly mirrors the experimentally observed interference tolerance and selectivity trends in electrochemical measurements.

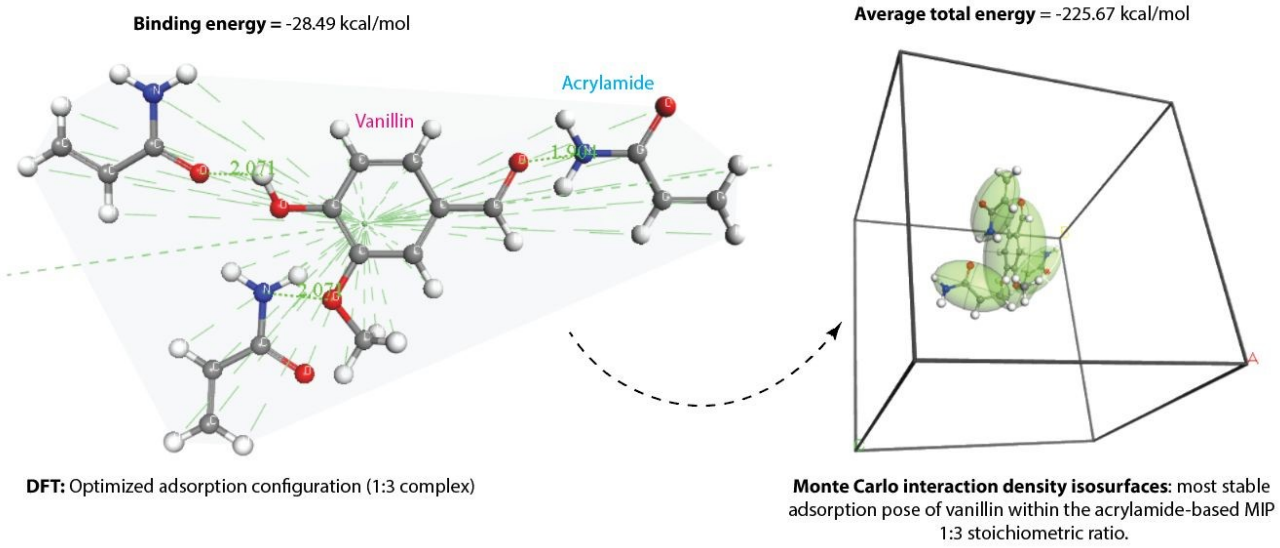

Fig.8: Optimized adsorption configuration and interaction mapping of vanillin within the acrylamide-based molecularly imprinted polymer (MIP) at a 1:3 stoichiometric ratio.

View Article Online
DOI: 10.1039/D6AY00358C

It is important to note that while these DFT-calculated binding energies successfully predict the thermodynamic preference of the imprinted cavities for vanillin over interferents like ascorbic acid (AA), they do not entirely dictate the experimental selectivity. As observed in the interference studies, AA still produces a pronounced overlapping electrochemical signal despite its lower binding affinity (−20.23 kcal/mol). This divergence between computational thermodynamics and experimental reality is governed by reaction kinetics and mass transport. Because AA is a small, highly hydrophilic molecule, it does not require specific coordination within the imprinted cavities to penetrate the sensor surface; rather, it rapidly diffuses through the non-specific interstitial pores of the polymer matrix. Furthermore, AA possesses a notoriously low oxidation overpotential on transition metal oxides, allowing it to easily undergo electro-oxidation once it reaches the internal Co_3O_4/TiO_2 surface. Therefore, while the imprinting process successfully instills rigid thermodynamic selectivity for vanillin, kinetic factors—specifically the rapid diffusion of small, highly electroactive species—must be accounted for when applying the sensor to complex matrices rich in vitamin C.

3.9.4. DFT–Electrochemical Signal Transduction Mechanism

The strong and highly oriented vanillin–acrylamide interactions identified by DFT provide a direct molecular-level explanation for the experimentally observed electrochemical signal amplification in the MIP/Co_3O_4/TiO_2 sensor. The optimized 1:3 complex exhibits a highly negative interaction energy ($\Delta E = -28.49$ kcal mol^{-1}), enforcing stable adsorption and precise orientation of vanillin within the imprinted cavities formed according to the mechanism depicted in **Scheme 1**. This molecular preorganization positions the phenolic and aldehydic redox-active moieties of vanillin in close electronic proximity to the Co_3O_4/TiO_2 p–n heterojunction, facilitating efficient charge delocalization and interfacial electron transfer.

View Article Online
DOI: 10.1039/D6AY00358C

Experimentally, this translates into a pronounced enhancement in anodic peak current and a high imprinting factor derived from cyclic voltammetry (IF_{CV}), confirming that signal amplification is governed by molecular recognition rather than nonspecific surface adsorption. Consistently, electrochemical impedance spectroscopy reveals a substantial decrease in charge-transfer resistance for the MIP-modified electrode (R_{ct} = 35.8 Ω·cm²) relative to the non-imprinted counterpart, in agreement with the DFT-predicted low deformation energies and favorable charge-transfer pathways across the polymer–electrode interface.

By contrast, glucose and ascorbic acid exhibit weaker interaction energies (−12.57 and −20.23 kcal mol^{-1}, respectively), leading to transient or misoriented adsorption that fails to establish sustained electronic coupling with the electrode. As a result, these interferents induce negligible changes in peak current and do not contribute to IF_{CV} enhancement, despite their intrinsic electrochemical activity. Collectively, the integrated DFT–electrochemical analysis confirms that the exceptional selectivity and sensitivity of the sensor originate from imprinting-induced, energetically favored adsorption that lowers the kinetic barrier for charge transfer, rather than from nonspecific catalytic oxidation on the metal oxide surface.

3.10. Comparative Analytical Performance

As summarized in **Table 2**, the proposed MIP/Co_3O_4/TiO_2 sensor demonstrates a highly competitive analytical profile relative to recently reported vanillin sensors based on catalytic nanomaterials, carbon architectures, and imprinting strategies. While several DPV- and SWV-based platforms achieve ultralow detection limits in simplified matrices (e.g., ZnCr-LDH@g-CN, MIP/RGO, MIG-CuS@COOH-MWCNTs), these systems typically exhibit narrower linear ranges, shorter operational stability, or reliance on advanced pulse techniques. In contrast, the present sensor achieves a broad linear range (2.5–250 μM)—capable of covering the concentration

View Article Online
DOI: 10.1039/D6AY00358C

variations typical of commercial food products without requiring extensive sample dilution—and a low LOD (0.06 μM) using conventional cyclic voltammetry. This underscores the intrinsic signal amplification provided by the p–n Co_3O_4/TiO_2 heterojunction combined with molecular imprinting.

Importantly, unlike many reported sensors validated only in single or low-complexity matrices or relying purely on spiked buffer systems, the proposed platform was systematically evaluated across diverse real food systems, including high-fat (milk, ice cream), carbohydrate-rich (biscuits), and polyphenol-rich beverages (coffee, iced tea). Because of the proven antifouling resilience of the MIP layer, the sensor successfully maintains high sensitivity without suffering from cumulative fouling, even in these highly complex, unspiked environments. The extended storage stability (42 days) further exceeds most reported MIP-based vanillin sensors, where polymer aging or surface fouling typically limits usability to ≤30 days. Collectively, these results position the MIP/Co_3O_4/TiO_2 sensor as a robust, mechanistically rationalized, and practically deployable alternative for selective vanillin determination in complex food matrices.

Table 2. Comparison of the proposed MIP/Co_3O_4/TiO_2 electrochemical sensor with recently reported vanillin sensors

Sensor material / configuration	Technique	Linear range (μM)	LOD (μM)	Matrix tested	Selectivity strategy	Stability	Ref.
MIP/Co_3O_4/TiO_2/GCE	CV	**2.5–250**	**0.06**	Milk, ice cream, biscuits, coffee, iced tea	Molecular imprinting + p–n heterojunction	**42 days**	This work
ZnCr-LDH@g-CN	DPV	0.001–143.2	0.009	Water, ice cream, chocolate	Catalytic oxidation	—	[40]
poly(MO)/PGE	DPV	1.0–26.0	0.10	Vanilla ice cream powder	Surface adsorption	—	[41]

View Article Online
DOI: 10.1039/D6AY00358C

CuHCF thin film	CV	0.76–120	0.23	Roasted coffee beans	Catalytic oxidation	30 days	42
MIP/RGO/GCE	SWV	0.00001–100	5.4×10^{-6}	Commercial infant formula	Molecular imprinting + reduced graphene oxide	11 days	33
CMP-rGO/GCE	DPV	0.08–33	0.014	Human serum, human urine, vanillin tablet	Catalytic oxidation	7 days	43
MIG-CuS@COOH-MWCNTs/GCE	DPV	0.03–125	0.006	Liqueur, white vinegar, vanilla ice cream	Molecular imprinting + carboxylated carbon nanotubes	30 days	44
CTABMGPE	DPV	4–70	1.29	Biscuit, beverage	Mixed adsorption/catalysis	—	45
PTOMCNPE	CV	2–40	0.093	Biscuit	Mixed adsorption and catalytic oxidation	7 days	46

ZnCr-LDH@g-CN: ZnCr-layered double hydroxide@g-CN; poly (MO)/PGE): poly (methyl orange) modified pencil graphite electrode; CuHCF thin film: modified copper hexacyanoferrate film; MIP/RGO: molecularly imprinted polypyrrole nanowires/reduced graphene oxide; CMP-rGO: benzopyrazine-based polymer coating on graphene; SWV: square-wave voltammetry; DPV: differential pulse voltammetry; MIG-CuS@COOH-MWCNTs: copper sulfide carboxylated carbon nanotubes molecularly imprinted polymer; CTABMGPE: ionic surfactant modified graphene paste electrode; PTOMCNPE: poly (titan yellow) and octoxynol-9modified carbon nanotube paste electrode.

4. Conclusion

A selective and mechanistically rational electrochemical sensor for vanillin determination was successfully constructed by integrating molecular imprinting with a Co_3O_4/TiO_2 p–n heterojunction. The oxide heterostructure provides an efficient electron-transfer backbone, while the imprinted polymer layer introduces molecular selectivity without compromising electrochemical accessibility. Systematic electrochemical analysis demonstrated that the imprinted architecture preserves charge-transfer kinetics and electroactive surface area while enabling target-specific accumulation at the sensing interface.

View Article Online
DOI: 10.1039/D6AY00358C

Density functional theory and adsorption simulations revealed that vanillin interacts optimally with acrylamide-based binding sites through a cooperative hydrogen-bonding network, with maximum stabilization at a 1:3 vanillin-to-monomer ratio. The markedly higher binding energy relative to glucose and ascorbic acid explains the experimentally observed selectivity and the elevated imprinting factors derived from cyclic voltammetry and impedance spectroscopy. This direct correlation between molecular-level interactions and macroscopic electrochemical performance confirms that DFT calculations serve as a predictive and explanatory tool rather than a descriptive add-on.

The sensor delivered a broad working range, low detection limit, excellent reproducibility, and long-term stability, and was validated across diverse real food matrices with results comparable to chromatographic reference methods. From an analytical perspective, the platform satisfies key requirements for food additive monitoring, including sensitivity well below regulatory concentration limits and resilience against complex matrix interference. More broadly, this study highlights how coupling heterojunction-driven electrochemical amplification with molecular imprinting and computational insight can enable the rational design of next-generation selective sensors for complex chemical environments.

View Article Online
DOI: 10.1039/D6AY00358C

CRediT authorship contribution statement

Favour Ezinne Ogulewe: Formal analysis, Investigation, Data curation, Writing – original draft. **Akeem Adeyemi Oladipo**: Methodology, Conceptualization, Validation, Writing – review & editing, Supervision, Project administration. **Mustafa Gazi**: Project administration, Validation, Supervision.

Declaration of competing interest

The authors state that they do not possess any identifiable conflicting financial interests or personal ties that could have potentially influenced the findings presented in this paper.

Data availability

Data will be made available on request.

Funding

The authors did not receive support from any organization for the submitted work.

References

1 M. Aghaziarati and H. Sereshti, *ACS Food Science & Technology*, 2025, **5**, 578–588.
2 A. Pravi, M. Rashid, V. Singh, S. Pandey, K. Sonika, P. K. Rao and S. K. Singh, *Analytical Methods*, 2025, **17**, 8716–8723.
3 C. I. Fort, S. C. A. Cobzac and G. L. Turdean, *Food Chem.*, 2022, **385**, 132711.
4 G. K. Ziyatdinova, A. S. Zhupanova and H. C. Budnikov, *Journal of Analytical Chemistry*, 2022, **77**, 155–172.
5 A. Umar, S. Hussain, S. A. Ansari, A. A. Ibrahim, M. A. M. Alhamami, T. Almas and S. Akbar, *Ceram. Int.*, 2025, **51**, 16037–16045.
6 S. A. Ansari, Z. Khatoon, N. Parveen, H. Fouad, A. Kulkarni, A. Umar, Z. A. Ansari and S. G. Ansari, *Sci. Adv. Mater.*, 2017, **9**, 2032–2038.
7 S. A. Ansari, N. S. Lopa, N. Parveen, A. A. Shaikh and Md. M. Rahman, *Analytical Methods*, 2020, **12**, 5562–5571.
8 M. Adeel, K. Asif, F. Alshabouna, V. Canzonieri, Md. M. Rahman, S. A. Ansari, F. Güder, F. Rizzolio and S. Daniele, *Biosens. Bioelectron. X*, 2022, **12**, 100256.
9 Z. Fan, L. Yuan, T. Xia, C. Zhao, W. Guo, A. A. Ibrahim, S. A. Ansari and A. Umar, *Microchimica Acta*, 2025, **192**, 167.

View Article Online
DOI: 10.1039/D6AY00358C

10 R. Ali, H. Elfadil, N. Sirag, R. Alshaman, A. S. Albalawi, N. Albalawi, A. albalawi, S. Alharbi, A. Al-anzi, S. alatawi, Y. Alhuaiti, N. Aldwsari and M. M. El-Wekil, *Microchimica Acta*, 2025, **192**, 469.
11 A. O. Alqarni, R. A. A. Alqahtani, A. M. Mahmoud, M. H. Almabadi, F. M. Alshareef, M. N. Goda, R. Ali and M. M. El-Wekil, *Microchemical Journal*, 2025, **218**, 115794.
12 R. Ali, A. Z. A. Albalawi, A. H. Alahmadi, N. M. Alanazi, A. M. Humadi, M. H. Alatwi, A. H. Alharbi, E. M. Albalawi, F. M. Albalawi and M. M. El-Wekil, *Microchemical Journal*, 2026, **220**, 116362.
13 H. Ansari and A. A. Oladipo, *Microchemical Journal*, 2026, **224**, 117839.
14 C.-B. Yu, C. Xu, L. He, W.-Y. Huang, K. Yang and D. Li, *J. Environ. Chem. Eng.*, 2025, **13**, 119195.
15 J. S. Raja, A. Rahim, S. Sabahat, M. Tariq, J. Iqbal, D. Fouad, A. Qadeer and F. S. Ataya, *Journal of Food Composition and Analysis*, 2025, **148**, 108220.
16 Q. Wang, L. Li, Y. Chai, Y. Hu and J. Liang, *The Journal of Physical Chemistry C*, 2023, **127**, 5358–5365.
17 M. Ganesan, R. K. Devi, A. S. Pillai, C. C. Lin, Y.-Y. Lee, B.-W. Huang, N. Sengottuvelan and G.-P. Chang-Chien, *Colloids Surf. A Physicochem. Eng. Asp.*, 2025, **725**, 137710.
18 B. Pan, S. Wang, G. Li and L. Zou, *Microchimica Acta*, 2025, **192**, 730.
19 A. Ramzannezhad, S. Ghasemi, B. Eftekharinia and S. Safari, *Sci. Rep.*, 2025, **15**, 37624.
20 R. Vivekananth, R. Suresh Babu, R. Atchudan, Y. Sasikumar, A. L. F. de Barros and R. Kalaivani, *Synth. Met.*, 2025, **311**, 117829.
21 F. E. Ogulewe, A. A. Oladipo and M. Gazi, *Talanta Open*, 2025, **11**, 100448.
22 L. Wang, M. Pagett and W. Zhang, *Sensors and Actuators Reports*, 2023, **5**, 100153.
23 A. Fallah, A. A. Oladipo, F. Khosravi and S. Pirgalıoğlu, *Int. J. Biol. Macromol.*, 2025, **329**, 147760.
24 I. Nompetsheni, N. Palaniyandy, N. W. Hlongwa and X. Fuku, *Microchimica Acta*, 2025, **192**, 708.
25 A. I. M. Rabee, C. B. A. Gaid, G. A. H. Mekhemer and M. I. Zaki, *Mater. Chem. Phys.*, 2022, **289**, 126367.
26 S. Ahmed, Md. K. H. Shishir, Md. T. Islam, Md. A. Rahaman, S. Aman, A. R. Aidid, S. I. Sadia, Md. M. Rana and Md. A. Alam, *Results in Materials*, 2025, **26**, 100673.
27 O. Sadek, S. Touhtouh, M. Rkhis and A. Hajjaji, *Inorg. Chem. Commun.*, 2024, **161**, 112092.
28 C. Fang, C. Wu and X. Zhao, *Int. J. Adhes. Adhes.*, 2023, **125**, 103403.
29 A. Saka, L. T. Jule, B. Badassa, L. Gudata, N. Nagaprasad, R. Shanmugam, L. P. Dwarampudi, V. Seenivasan and K. Ramaswamy, *BMC Chem.*, 2024, **18**, 123.
30 P. Tharasan, M. Somprasong, N. Kenyota, N. Kanjana, W. Maiaugree, W. Jareonboon and P. Laokul, *Journal of Nanoparticle Research*, 2022, **24**, 126.
31 L. Wang, G. Tang, S. Liu, H. Dong, Q. Liu, J. Sun and H. Tang, *Chemical Engineering Journal*, 2022, **428**, 131338.
32 W. Liu, Z. Zhang, M. Qi, W. Wu, J. Sun, Z. Li and Z. Wang, *Microchimica Acta*, 2026, **193**, 67.
33 Y. Feng, H. Guo, G. Zhang, Y. Zhu and S. Wu, *Microchemical Journal*, 2024, **205**, 111248.

View Article Online
DOI: 10.1039/D6AY00358C

34 I. Kouhi, G. Parvizi Fard, E. Alipour and A. Saadatirad, *J. Food Process. Preserv.*, DOI:10.1111/jfpp.16289.
35 T. Tabanlıgil Calam and G. Taşkın, *Food Chem.*, 2024, **436**, 137752.
36 S. Dehdashtian, S. Wang, T. A. Murray, M. Chegeni, S. Rostamnia and N. Fattahi, *Sci. Rep.*, 2023, **13**, 17907.
37 Y.-Y. Lee, B. Sriram, S.-F. Wang, M. M. Stanley, W.-C. Lin, S. Kogularasu, G.-P. Chang-Chien and M. George, *Applied Surface Science Advances*, 2024, **20**, 100584.
38 A. Venkadesh, J. Mathiyarasu and S. Radhakrishnan, *Mater. Today Chem.*, 2021, **22**, 100554.
39 Y. Qiao, L. Tan, J. Zhao, J. Wang and H. Liu, *Microchimica Acta*, 2026, **193**, 16.
40 S. Gopi and S.-F. Wang, *Microchimica Acta*, 2023, **190**, 423.
41 E. Pradeepa, Y. Arthoba Nayaka and N. R. Manjushree, *Mater. Chem. Phys.*, 2023, **296**, 127180.
42 P. Prabhu, R. S. Babu and S. S. Narayanan, *Journal of Materials Science: Materials in Electronics*, 2019, **30**, 9955–9963.
43 X. Li, Y. Fang, H. Li and S. Feng, *Talanta*, 2024, **277**, 126420.
44 Y. Chen, Y. Sun, G. I. N. Waterhouse, H. Gao and Z. Xu, *Sens. Actuators B Chem.*, 2023, **377**, 133045.
45 C. Raril and J. G. Manjunatha, *Microchemical Journal*, 2020, **154**, 104575.
46 G. Tigari, J. G. Manjunatha, E. S. D'Souza and N. Sreeharsha, *ChemistrySelect*, 2021, **6**, 2700–2708.

View Article Online
DOI: 10.1039/D6AY00358C

Data availability

Data will be made available on request.